DRAG REDUCTION MECHANISMS DERIVED FROM SHARK SKIN

ICAS-86-1.8.3

by

D. W. Bechert, M. Bartenwerfer, G. Hoppe
DFVLR, Mueller-Breslau-Str. 8, 1000 Berlin 12, FRG

and

W.-E. Reif, Institut fuer Geologie und Palaeontologie der Universitaet,
Sigwartstr. 10, 7400 Tuebingen, FRG

Abstract

A variety of drag reducing mechanisms of shark skin are considered. In terms of fluid dynamics these are based on either:

(a) a delay of separation by shear-stress dependent mixing control of the turbulent boundary layer or

(b) a reduction of turbulent shear stress below the value of a smooth surface.

First, we give a survey on possible mixing control mechanisms (a) which can be attributed to the structures which we find on shark skin. Although these mechanisms are plausible, only few laboratory data are available to support these ideas.

On the other hand, turbulent shear stress reduction of 7-8% below the value of smooth surfaces (b) has been demonstrated independently in several laboratories. These drag reducing surfaces exhibit small longitudinal riblets. Spacing and height of the tiny riblets have dimensions comparable to the dimensions of the viscous sublayer of a turbulent boundary layer. In addition, these tiny riblets are found on the scales of all species of fast sharks.

The idea of the shear stress reduction mechanism by riblets is this: There are small streamwise vortices in the viscous sublayer of a turbulent boundary layer. The streamwise vortices produce a local upwash of slow fluid away from the surface. This is equivalent to the occurence of low speed streaks. The velocity profile in a low speed streak is highly unstable and this causes the high fluctuation activity (bursts) in the layer adjacent to the viscous sublayer. Thus, the streamwise vortices should be hampered in order to decrease turbulent mixing and hence decrease the turbulent shear stress. This can be achieved by small longitudinal riblets which impede the cross flow of the streamwise vortices. The riblets should have a finer lateral spacing than the spacing of the streamwise vortices.

The thrust of the present paper is to devise a theory of the viscous flow on surfaces with small longitudinal riblets. Therefore, in our analytical model, we consider various riblet shapes immersed in a viscous Couette type shear flow. The height by which the riblets protrude into the boundary layer flow is of crucial importance. This protrusion height cannot be increased beyond a certain level for all conceivable straight riblet configurations. The limit for the protrusion height is the essential finding of the present investigation. In addition, fairly detailed flow data on various riblet configurations are given. These include sawtooth, blade-like, scalloped and convex riblet cross sections. The analytical calculations are confirmed by electrolytical analogy experiments.

In order to circumvent the limit for the protrusion height of the riblets, staggered short riblets are suggested. By electrolytical analogy experiments, it is shown, that the protrusion height of this novel device may be increased to more than twice the value of conventional straight riblets. Finally, it is documented, that the skin of fast sharks clearly exhibits already the suggested short staggered riblets.

1. Survey of previously suggested mechanisms

The properties and the drag reduction mechanisms of shark skin are distinctly different from those of other marine animals such as, e.g., the compliant skin of dolphins, which is considered to delay transition [1,2]. The mucus of bony fish is another very efficient means to reduce fluid dynamical drag in water [3]. However, on the surface of sharks one sees only extremely small amounts of mucus if one compares it with the surface of bony fish. Thus, for the time being, we use as a working hypothesis*) that mucus is probably not essential for the drag reduction of sharks and hence we are looking for other mechanisms there.

Bone [5] has suggested that the peculiar shape of the scales on spiny dogfish, a species of sharks, may serve as vortex generators. Vortex generators would enhance mixing in the turbulent boundary layer on the body of the fish and thus help keeping the flow from separating. Certainly, separation control is essential for sharks, since sharks are obviously not only in steady forward motion. Unfortunately, spiny dogfish is a slow shark and scales of slow sharks are very dissimilar to those on fast sharks [6]. For slow sharks, other biological functions like, e.g., protection against parasites or abrasion are of paramount importance. To demonstrate the differences, Fig. 1 shows the scale patterns on a fast shark, the silky shark. Fig. 2 shows the scales of a slow shark, the bramble shark.

For our considerations we focus on the scales of fast sharks only. A typical survey of the shapes of the scales on a fast shark, a Galapagos shark, is given in Fig. 3. On the snout (rostrum) of the shark, the scales look like well adjusted paving stones with a very smooth surface. A similar structure we see at the leading edge of the pectoral

*) This issue has been discussed in more detail in our previous paper [4].

fins. In these two locations laminar flow and varying flow directions due to varying stagnation point locations can be assumed. In the middle of the body and the fins we recognize an anvil-like structure of the scales, with ridges in the downstream direction. It looks, as if the direction of the ridges follows the local flow direction [7]. However, this specific orientation of the scales is lost in scars [8]. On the rear part of the body and the fins, the scales look like little hands and these are less rigidly anchored in the skin as the anvil-like scales are. On some species of very fast sharks, like the hammerhead sharks and the mako, the body is almost completely covered with very small hand-like scales.

For fast off-shore sharks, the dimensions of the scales lie between 0.2 and 0.5 mm. The lateral spacing of the ridges on the crown of the scales is between 0.035 and 0.1 mm. The scales carry between 3 and 7 ridges; the larger scales on silky shark and Galapagos shark exhibit the larger numbers, i.e., 7 ridges.

There are only sparse data on the velocities of fast sharks. The burst speeds are in the range of 10-15 m/s [4,9]. The cruise speeds are lower; we estimate about 2-5 m/s. Data on the size of each species can be found in the literature [10,11]; a typical length of a fast shark is about 2-3 m, with white sharks growing to about 6 m length. The Reynolds number, calculated with the body length lies in the 10^6-10^7 order. Thus, it is reasonable to assume turbulent flow on most parts of the surface of a fast shark. In the following, we will discuss a number of conceivable and previously suggested fluid dynamical mechanisms related to shark scales.

1.1. Separation control

1.1.1. Shark scales with V-shaped ridges

Separation control by enhanced mixing of the turbulent boundary layer is useful in regions of strong positive pressure gradients where separation is likely to occur. The pectoral and caudal fins of sharks have airfoil profiles and operate, roughly speaking, similar to the blades of a turbomachine. Thus, on the surface of the fins, from about half the chord length on, we may look for patterns which help to keep the flow attached. Indeed, there we find for several species scales with a V-shaped central ridge (see Fig. 4). Such structures produce enhanced mixing by the generation of streamwise vortices [4] with an upwash of fluid downstream of the V-shaped wedge.

1.1.2. Shark scales at an angle of attack

Our previous investigations on shark scales with different angles of attack were caused by our observation, that on the skin of dead sharks of some fast species (e.g., mako and hammerhead shark) the angle of attack of the scales is not defined. The individual hand-like scales can attain different attitudes within an angle regime of, say, 0 and 30 degrees. Therefore, we have carried out experiments with artificial surfaces with "scales" at different angles [4]. The essence of the results was, that there is a dramatic increase of turbulent shear stress with an only small increase of angle of attack of the individual scales. Since enhanced turbulent shear stress is equivalent to enhanced mixing, it is obvious, that turbulent mixing can be controlled efficiently by small changes of the scale angles. Conceptually, there are two possibilities for a passive separation control mechanism:

(a) Elastically anchored scale: we assume that the scales are elastically anchored with the zero position at an angle of attack of, say 10°-20°. Under normal shear stress conditions, the scales are assumed to be aligned completely at an angle of 0°. For decreasing shear stress, however, which is typical for a flow close to separation, the scales will pop up and will increase turbulent mixing. Thus, separation can be delayed.

One open question is, however, how well this mechanism responds to varying flow speeds. If there is a coupling between anchoring stiffness of the scales and speed of the animal via tension of the skin [12], then this can be considered as a plausible mechanism. Nevertheless, it is difficult to imagine how this will work on the surface of the fins.

(b) Loosely suspended scale with passive flow control: There is another possibilty of a direct fluid-dynamically operated control of the angle of attack of the scales. The scales in the rear part of the body and the fins are hand-shaped. There is a cavity underneath the surface, connected over a significant area. The individual scales have also a significant vertical surface. In Fig. 5 a schematic view of an array of hand-like scales can be seen. Assume now a flow with positive pressure gradient in the streamwise direction, i.e., a flow close to separation. The positive pressure gradient produces a reversed secondary flow underneath the surface (see Fig. 5). This secondary flow causes a drag force on the vertical surface of each scale. This force increases the angle of attack of the scales if the shear stress decreases significantly. As before, a situation close to separation leads to an increased mixing and hence separation is delayed. We have suggested this separation control recently in a patent [13]. Neverthless, a complete verification of this suggested mechanism in the laboratory has not yet been carried out.

In the above discussion we have considered methods to enhance mixing for separation control. Unavoidably, enhanced mixing produces also increased shear stress drag. Thus, enhanced shear stress drag can be tolerated only if avoiding separation is of paramount importance in a certain region of a body immersed in fluid. Thus, enhanced mixing on demand, as proposed here, looks promising.

If separation is no problem, shear stress reduction is preferable. This issue will be discussed in the following section.

1.2. Turbulent shear stress reduction

1.2.1. Basic fluid dynamics

Fig. 6 shows the flow structure of a turbulent boundary layer as seen through a transparent wall [14,15]. The fluid is water and the flow structure is made visible by aluminum particles. What we see is the viscous sublayer of the turbulent boundary layer. One can recognize easily a streaky structure in the downstream direction. The typical lateral spacing λ_z of the streaks is $\lambda_z^+ \approx 100$ [16,17]. ex-

pressed in wall units*). The streaks in Fig. 6 are produced by slowly rotating streamwise vortices. The streamwise vortices provide a transport mechanism of slow fluid being convected away from the surface and fluid of high velocity taken back to the surface. The regions of slow fluid, the "low speed streaks" have been detected first with hydrogen bubble flow vizualization in water [16].

Macroscopic momentum transport across the boundary layer is the cause of the high shear stress of turbulent boundary layers as opposed to laminar boundary layers. The streamwise vortices contribute to this momentum transport, but they produce also distortions of the mean velocity profile (i.e., the low speed streaks). These distortions cause high local instabilities ("bursts" [18]), which are responsible for the high turbulence activity close to the wall.

Recently, Jang, Benney and Chen [19] provided a convincing theory for the streamwise vortices. They assume the mean velocity profile of a turbulent boundary layer and calculate possible flow instabilities. There are two classes of instability modes which coincide at a certain wavelength and frequency. The nonlinear interaction of these two wave types produces a secondary flow in form of longitudinal vortices, whose streamlines had been also calculated (see Fig. 7). The lateral wavelength is predicted very well, i.e., the theoretical result is $\lambda_z^+ = 90$. The question, however, as to what the streamwise wavelength is, does not seem to be settled completely. The theory [19] predicts $\lambda_x^+ = 338$. On the other hand, the available hydrogen bubble vizualization data suggest a higher value, between $\lambda_x^+ \approx 630$ [20] and $\lambda_x^+ > 1000$ [17]. We feel, however, that the evaluation of a streamwise wavelength from hydrogen bubble data is difficult and certainly less reliable than the measurement of the lateral wavelength λ_z^+ by the same method.

1.2.2. Riblet surfaces

The fluid dynamical idea of turbulent shear stress reduction by surface modifications is the following: In order to hamper the development of the streamwise vortices fine riblets with sharp ridges are arranged on the surface and oriented in the streamwise direction. These riblets impede the lateral flow component of the vortices. As a consequence thereof, the vortex cores move a bit farther away from the surface. Thus, the viscous sublayer grows thicker, which is equivalent to a reduced shear stress [21]. In addition, the turbulence fluctuation level is reduced in the vicinity of the wall [22]. We have carried out similar measurements. Fig. 8 shows a comparison of hot wire data above a smooth flat plate and above a riblet surface. The drag reduction of the riblet surface is 6%, measured independently by a direct shear stress measurement (the method is described in [4]). The changes in the mean velocity profile are very minor and not shown here; the mean flow distribution is only shown to clarify where we are in the boundary layer. More interesting are the deviations in the fluctuation level u'_{RMS}.*) The turbulent shear stress $\tau = \rho\, \overline{u'v'}$ is a quadratic quantity in terms of the fluctuations. This quantity is reduced by 6%. Thus, we should expect a reduction in the fluctuation level, which is a linear quantity, of 3%. And this is exactly what we see in the region not too far from the wall, where the shear stress does not differ very much from the value just at the wall. This measurement shows, that the effects of a drag reducing surface on the turbulence are by no means dramatic.

A typical measurement with a shear stress reducing surface is shown in Fig. 9. D/D_{FP} on the vertical axis is the drag of the riblet plate divided by the drag of the smooth flat plate. We see a drag reduction for values of the dimensionless**) lateral riblet spacing s^+ being smaller than the spacing of the streamwise vortices, $s^+ < \lambda_z^+/2 \approx 35$–$50$. Sawtooth riblets show a similar behaviour [23] as the scalloped riblets in Fig. 9, which exhibit a 7 - 8% drag reduction. In Walsh's [23] and our experiments, it has turned out, that it is crucial that the edges of the riblets are sharp. Convex riblets with rounded ridges have no drag reducing effect [23]. The ridges on the scales of fast sharks have always sharp edges [6]. As we have shown in previous papers [4,7], the lateral spacing of the riblets on shark scales have, roughly estimated, the "right" spacing. We will return to the fluid dynamics of riblet surfaces in more detail in section 2 of this paper.

1.2.3. Low speed streak cancellation by fluid ejection

Whereas we were on comparatively solid ground with the preceding two subsections of this paper, the following suggested mechanism is only supported by analytical estimations and by observations on the structures of shark skin. From some sparse and, admittedly, not completely satisfactory data from the literature [24] and from analytical considerations [4], we concluded that the "low speed streak" regions in the viscous sublayer should be at the same time regions of lower instantaneous static pressure. We suggest to install small slits in the surface with their exit in the downstream direction. Due to the low pressure in the "low speed streak" region, fluid should be ejected through the slits in the downstream direction. In this way the velocity defect of the "low speed streaks" could be compensated, at least partly [4]. Such a surface with slits could look, in longitudinal cross section, like the device shown in Fig. 10. The cavities underneath the surface are connected. The particular surface in Fig. 10 exhibits also longitudinal riblets for improved performance. Incidentally, this is a longitudinal cross section through actual shark skin with anvil-like scales (see Fig. 3). This, admittedly, still speculative mechanism can be extended even further. With the slits of Fig. 10 we inject fluid in the downstream direction in order

*) The quantity λ_z^+ is a Reynolds number, calculated with the shear stress velocity $\sqrt{\tau_0/\rho}$. We have $\lambda^+ = \lambda \cdot \frac{\sqrt{\tau_0/\rho}}{\nu}$. τ_0 is the shear stress of a smooth flat plate; ρ and ν are the density and the kinematic viscosity of the fluid, respectively.

*) In this measurement, the hot wire length was l = 1.36 mm, in wall units $l^+ = 76$, i.e., not small enough to pick up the full fluctuation level very close to the wall. However, a comparison before/ after is still sufficiently conclusive.

**) The riblet spacing s is expressed in wall units, i.e., $s^+ = s \cdot \sqrt{\tau_0/\rho}/\nu$ · s^+ is roughly proportional to the mean flow velocity.

to compensate the u'-defect in the instantaneous velocity profile. However, the induced flow of the streamwise vortices does not only posess a u' down-stream component, but also a w' cross flow component (see Fig. 7). Therefore, an ejection of fluid to the sides should be also advantageous. A device to achieve this could look like the array of plates in Fig. 11, which is a lateral cross section as Fig. 7 is. Since the location of the low speed streaks is not fixed, an array of plates like in Fig. 11 should be adjusted instantaneously. If the individual plates or scales are anchored elastically, this can be achieved in a simple way: In the regions of the low speed streaks, the shear stress is lower and the scales pop up to a higher angle of attack. Also, the above mentioned static pressure difference has the same effect on a scale with hand-like shape. In our previous paper [4], we have estimated the time constants of such a mechanism and we have found compatible time constants for (a) the fluid motion of the low speed streaks and (b) the mechanical reaction of the shark scales. On the other hand, the same estimation of time constants [4] shows, that the latter mechanism utilizing compliant scales works only in liquids and not in gases.

2. The viscous flow on riblet surfaces.

2.1. Basic equations

The reader may have realized from the preceding sections how many plausible mechanisms are conceivable and, on the other hand, how difficult it may be to prove most of them. In order to get some unambiguous information, for a change, we will perform a rigorous viscous flow analysis. Eventually, this will lead to new insights which could not have been obtained by just intelligent speculations accompanied by rough estimations.

One of the unsettled questions of riblet surfaces is as to where the apparent (average) origin of the velocity profile might be located. This question was raised by Hooshmand et al. [21] and we suggested in our previous paper [4] that this problem could be solved analytically by a viscous flow theory. In Fig. 12 we show what we mean with the term "apparent origin". It is that particular elevation where the boundary layer "sees" an equivalent smooth wall. Another way to interpret the apparent origin is to consider it as the center of gravity of the shear stress distribution on the riblet surface. At first glance, this appears as an academic discussion. However, it is of paramount importance how far the ridges protrude above this apparent origin (see Fig. 12). This *protrusion height* determines how far the flow above the riblet surface can be influenced by the riblets. An optimization of the riblet shape is at the same time an optimization for maximal protrusion height*).

Thus, we consider the average mean flow of the viscous sublayer in which the riblet surface is immersed. In the following equations we choose x as the direction of the mean flow. The 1st Navier-Stokes equation is

$$\frac{\partial u}{\partial t} + u\frac{\partial u}{\partial x} + v\frac{\partial u}{\partial y} + w\frac{\partial u}{\partial z} + \frac{1}{\rho}\frac{\partial p}{\partial x} = \nu\nabla^2 u \ . \qquad (1)$$

*) With the constraint that the riblet spacing should be smaller ($\approx 1/2$) than the spacing of the streamwise vortices.

We assume a flat plate boundary layer flow without mean flow pressure gradient, so $\partial p/\partial x = 0$. If the riblet surface is immersed in the viscous sublayer, neglecting the convective terms on the left hand side of the equation is certainly a good approximation. Consequently, for 2-dimensional riblets we are left with the equation

$$\frac{\partial^2 u}{\partial y^2} + \frac{\partial^2 u}{\partial z^2} = 0 \ . \qquad (2)$$

This is the Laplace equation for the velocity u. To solve this equation in two dimensions, various established techniques can be used. One particularly suitable of them is conformal mapping, which will be used in the following section.

Before we will do this, however, we will discuss the basic equations for 3-dimensional riblets. Here, we can no more assume a priori that the pressure gradients are zero. For a viscous steady flow, we are left with

$$\left\{ \begin{array}{l} \frac{\partial p}{\partial x} = \mu\nabla^2 u \\ \frac{\partial p}{\partial y} = \mu\nabla^2 v \\ \frac{\partial p}{\partial z} = \mu\nabla^2 w \end{array} \right\} \ , \qquad (3)$$

where μ is the viscosity of the fluid. Taking derivatives of these equations, we can eliminate the pressure and obtain

$$\left\{ \begin{array}{l} \nabla^2\left(\frac{\partial u}{\partial y} - \frac{\partial v}{\partial x}\right) = 0 \ , \\ \nabla^2\left(\frac{\partial u}{\partial z} - \frac{\partial w}{\partial x}\right) = 0 \ , \text{ etc.} \end{array} \right\} \qquad (4)$$

First, we try trivial solutions for equations (4), such as

$$\nabla^2 u = 0; \quad \nabla^2 v = 0; \quad \nabla^2 w = 0 \qquad (5)$$

or

$$\left(\frac{\partial u}{\partial y} - \frac{\partial v}{\partial x}\right) = 0; \quad \left(\frac{\partial u}{\partial z} - \frac{\partial w}{\partial x}\right) = 0, \text{ etc.} \qquad (6)$$

Clearly, $\nabla^2 u = 0$ leads with eq. (3) to $\partial p/\partial x = 0$. If we use, on the other hand, the equations (6) to replace v and w in eq. (3), we have

$$\frac{\partial p}{\partial x} = \mu\frac{\partial}{\partial x}\left(\frac{\partial u}{\partial x} + \frac{\partial v}{\partial y} + \frac{\partial w}{\partial z}\right) \ . \qquad (7)$$

With the continuity equation

$$\frac{\partial u}{\partial x} + \frac{\partial v}{\partial y} + \frac{\partial w}{\partial z} = 0 \qquad (8)$$

we find again $\frac{\partial p}{\partial x} = 0$ or $\nabla^2 u = 0$.

We know, however, from other solutions of the viscous flow equations, that the pressure is most likely not constant in our flow field. In Stokes' solution, e.g., for the viscous flow on a sphere, $1/3$ of the drag force comes from the contribution of the pressure normal to the surface. On the other hand, in our investigations, we will deal only with blade-like structures aligned to the mean flow direction. Thus, the static pressure is not expected to contribute anything whatsoever to the fluid force on such a structure. Based in these conjectures, we submit, that a solution satisfying $\nabla^2 u = 0$ in three dimensions, and with $u = 0$ on the surface, will produce a shear force very similar to the one generated by the solution of the complete equations

(3) and (8).*) As we have mentioned already, the apparent origin of a structure with surfaces aligned with the flow, can be interpreted as the elevation of the center of gravity of the shear stress distribution. Thus, we estimate the protrusion height of a three-dimensional flow-aligned structure by a solution of the three-dimensional Laplace equation, $\nabla^2 u = 0$.

To solve the Laplace equation in 3 dimensions, again established methods are available, such as, e.g., a numerical source distribution approach. On the other hand, almost forgotten methods, like the electric field analogy in an electrolytic tank experiment can be also utilized. This latter method turns out to be simple and easy to handle. In particular, the protrusion height can be determined by a straight-forward electrolytic resistance measurement, as will be shown in section 4.

2.2. Two-dimensional riblets, conformal mapping

To solve viscous flow problems on 2-dimensional riblet surfaces, conformal mapping is superior to other methods. There are two striking advantages:

(a) Sharp edges which produce singularities in the flow field do not lead to problems or inaccuracies with this method, whereas, e.g., purely numerical methods would be in trouble there.

(b) For a variety of configurations, solutions in closed form can be worked out, in particular simple formulae for the protrusion height can be produced.

Conformal mapping utilizes the fact that for the equation

$$\frac{\partial^2 u}{\partial z^2} + \frac{\partial^2 u}{\partial y^2} = 0 \qquad (2)$$

arbitrary functions f(z + iy) are solutions, as one can verify easily. The function f, the mapping function, has to be selected so that the boundary condition on the riblet surface is u = 0. The mean flow u-distribution will be a uniform Couette shear flow in order to emulate the viscous sublayer. What we will do by conformal mapping is to transform a uniform shear flow above a smooth plane surface into that above the particular riblet surface. So the task is to do mathematically what we see in Fig. 13. By the way, the solid lines in Fig. 13 are not streamlines, but lines of constant velocity u (isotaches). In conformal mapping we usually plot the real and imaginary part of a function. So we obtain a network with lines intersecting each other perpendicularly. If the imaginary part of our function is u, what is then the significance of the real part, i.e., the broken lines in Fig. 13? The answer is simple: Between two broken lines a shear force

$$\Delta F = l \cdot \tau_0 \cdot \Delta z \qquad (9)$$

is transmitted. In equation (9), l is the length in the streamwise (x) direction and Δz is the spacing between two broken lines of the undisturbed grid far above the riblet surface. τ_0 is the shear stress $\tau_0 = \mu \cdot du/dy$, where du/dy is the velocity gradient above the smooth surface or far away from the riblet surface. Thus, we call the broken vertical lines in Fig. 13 force lines (isodynes).

*) Of course, we consider this only as a somewhat deficient approach for the time being, which should be replaced by a direct flow experiment and/ or a numerical solution of the full viscous flow equations.

2.2.1. Riblets with sawtooth shape

Riblet surfaces with sawtooth-like cross section have been extensively tested by Walsh [22,23] and they do produce drag reduction in a turbulent boundary layer. Therefore, we have chosen this configuration first for our viscous flow analysis. The procedures of the conformal transformations are as follows (see Fig. 13):

(a) A rectangular grid of velocity lines and force lines in the w_1-plane ($w_1 = z_1 + iy_1$) is fixed. The vertical extension of the grid is chosen from $y_1 = 0$ to an arbitrary upper value, and the horizontal extension z_1 is from $-\pi/2$ to $+\pi/2$.

(b) This grid is transformed by the mapping function sinus, i.e., $w_2 = \sin w_1$.

(c) The half-plane above a straight horizontal line can be transformed into the plane inside a polygon by virtue of the Schwarz-Christoffel transformation. For details on this technique see, e.g., the books of Betz [25] and Kober [26].

The Schwarz-Christoffel transformation provides the mapping function to relate the w_3-plane to the w_2-plane*):

$$\frac{dw_3}{dw_2} = C_1 \cdot \frac{1}{(w_2 + 1)^{\alpha/\pi}} \cdot \frac{1}{(w_2 - 1)^{(\pi-\alpha)/\pi}} \qquad (10)$$

C_1 is a constant and the integration of eq. (10) will produce another constant C_2. These two constants have to be determined later. α is the corner angle of the polygon (see Fig. 13). In order to carry out the integration, it is useful to introduce the following substitution

$$\xi = \left(\frac{w_2 - 1}{w_2 + 1}\right)^{\frac{1}{n}} \quad \text{with} \quad \frac{1}{n} = \frac{\alpha}{\pi} . \qquad (11)$$

We obtain

$$w_3 = n \cdot C_1 \int \frac{d\xi}{1 - \xi^n} + C_2 . \qquad (12)$$

This integration can be carried out for n being an integer number [27]. For n = 4 (α=45°), we obtain, e.g.,

$$w_3 = \frac{s}{2}\left[1 + \frac{i}{\pi}\left(\ln\frac{1+\xi}{1-\xi} + 2\arctan\xi\right)\right] \qquad (13)$$

with $\xi = \left(\frac{w_2 - 1}{w_2 + 1}\right)^{1/4}$. For this case, the constants had been determined as

$$C_1 = \frac{is}{2\pi} \quad \text{and} \quad C_2 = \frac{s}{2} \qquad (14)$$

in order to obtain a grid pattern with the dimension and orientation like in Fig. 13.

For other angles, the mapping function can become more cumbersome. However, we have worked out the mapping functions for:

n	3	4	6	8
α	60°	45°	30°	22.5°
ridge angle	120°	90°	60°	45°

*) This is a receipe-like procedure. Why equation (10) is valid, is explained in [25].

The formulae of the mapping functions are given in appendix A. The grid pattern, i.e., the velocity distributions and the force lines are given in Fig. 14 to 17. These drawings are computer plots of our equations. Several things become obvious from these plots:

(i) The velocity perturbations caused by the riblet structure are vanishing very rapidly with increasing distance from the riblet surface.

(ii) There is very little fluid motion and extremely low shear stress at the bottom of the grooves, in particular for the smaller riblet angles.

(iii) The protrusion height h_p does not seem to increase above a certain fraction of the riblet spacing s.

This latter observation can be quantified further. We track down through the coordinate transformations where the different points A, B and C move for a riblet surface, in comparison to the undisturbed reference pattern (represented by $\alpha = 90°$ or $n = 2$). In this way, we can derive a general formula for the protrusion height h_p for arbitrary riblet angles. The details of this calculation are given in appendix B. We find

$$\frac{h_p}{s} = \frac{\cot g\alpha}{2} + \frac{1}{2\pi}\left(\gamma + 2\ln 2 - \frac{\pi}{\alpha} + \psi\left(1+\frac{\alpha}{\pi}\right)\right) \quad (15)$$

In this equation, γ is the Euler constant $\gamma = 0.5772$ and ψ is the Digamma function, as defined and tabulated in the tables of Abramovitz & Stegun [28]. In Fig. 18 we have plotted equation (15) for the protrusion height versus the height of the riblets. Both quantities have been made dimensionless with the riblet spacing s. For low values of the relative riblet height h/s, the protrusion height is half the riblet height, i.e., $h_p \approx h/2$. For high riblets, however, there is a saturation of the protrusion height at $h_{p_{max}} = 0.2206\ s$. This saturation limit ($0.2206 = \ln 2/\pi$) is an important and unexpected finding of this paper. We will see in the next section whether or not this limit value is also valid for other configurations.

2.2.2 Blade shaped riblets

Two-dimensional blade-shaped riblets have been introduced by Wilkinson [29] as a drag reducing surface. Preliminary tests seem to show, that the turbulence levels above such a surface immersed in a turbulent boundary layer are lower than those on sawtooth shaped riblet surfaces [29]. Therefore, we carry out the viscous flow calculation also for this configuration.

As in the preceding section, the viscous flow on blade-shaped riblets can be calculated using the Schwarz-Christoffel transformation. In fact, a transformation with $n = 2$ (i.e., rectangular corners) and a shift in coordinates between the w_2 and the w_3 planes would do the job. However, the following procedure to solve the problem is different and ressembles somewhat the procedure to calculate the flow in blade rows of turbomachines [25]. Its basic advantage is that it can be modified to deal with other configurations such as scalloped riblet shapes, which are found on shark scales [4,6].

If we use methods of turbomachinery flows, we may draw the reader's attention to an obvious fact: The grids representing lines of u = const and F = const look like streamlines Ψ = const and potential lines Φ = const. In spite of the fact that we do not really consider a stream in the z,y-plane we may, however, utilize this analogy. This has the advantage, that, as fluid dynamicists, we are used to think in terms of streamlines. It is, e.g., easy to see what a stagnation point and a stagnation streamline in the Ψ,Φ-plane are. However, how would we call this in our u,F-plane? Thus, we will use Ψ and Φ instead of u and F, intermediately. At the end of our calculations, we will just change the names of the functions back to u and F, their real meaning.

In the Ψ,Φ-plane, the task is to find the flow around an array of blades. This task is carried out in several steps (see Fig. 19). The w_1-plane is not shown in Fig. 19. It is, as before, an undisturbed rectangular Ψ,Φ (or u,F) grid. The flow in the w_2-plane is the flow around a cylinder of radius a, induced by a vortex with strength Γ_o. The induced field of this vortex alone would be

$$\Phi + i\Psi = \frac{i\Gamma_o}{2\pi}\ln(z_2 + iy_2) \ . \quad (16)$$

In order to fullfill the no penetration condition on the surface of the cylinder, we need a mirror image vortex of identical strength Γ_o, but with negative sign, inside the cylinder at an excentric location E. Having only these two vortices would produce a field with circles as streamlines everywhere. Also, as we would see later, the streamlines in the final w_4-plane would not be these of a horizontal parallel flow. This latter condition is fullfilled if we install an additional positive vortex of strength Γ_o in the center of the cylinder.

We will not show all details of the mathematics here. Since there are no particular tricks involved, we will show only a few equations and outline the essential steps of the transformations. We find for the stream function of the flow around the cylinder in Fig. 19, which is the stream function of the sum of the three vortices:

$$\Phi + i\Psi = w_1 = \frac{i\Gamma_o}{2\pi}\ln\left[\frac{w_2\,(w_2 - 1)}{w_2 - 1 + a^2}\right] , \quad (17)$$

where $w_2 = z_2 + iy_2$. The radius of the cylinder is a and the distance between the origin at A (where the inducing vortex is located) and the center of the cylinder at M has been set equal to one.

The streamlines can be calculated by inverting equation (17) to find w_2 at a given w_1. Since (17) is a quadratic equation for w_2, this is a straightforward procedure. By following one Ψ = const line through the w_2-Plane, one can decide which one of the two solutions of the quadratic equation is to be chosen.

The next step is to "smash" the cylinder in Fig. 19 to obtain a single blade of finite length. The transformation capable to do that is well known from airfoil theory, i.e., the Kutta-Joukowsky transformation

$$w_3 = w_2 + \frac{a^2}{w_2} \ . \quad (18)$$

Before we apply this transformation, however, we have to shift the origin of the coordinate system from A to the center of the cylinder, M. Thus, with the appropiate adjustment of constants, we have

instead of eq. (18)

$$w_3 = (w_2 - 1) + \frac{a^2}{(w_2 - 1)} + 1 + a^2 \quad . \qquad (19)$$

After having applied the Kutta-Joukowsky transformation, the point A has moved a bit to left and, interestingly enough, the stagnation streamline $\Psi = 0$ still remains a circle.

Before performing the next step, we move the origin back to the (shifted) center of the inducing vortex, A. By applying the transformation ln w we obtain the desired periodical flow pattern on the blade row. With the proper choice of constants, the transformation equation is

$$w_4 = \frac{is}{2\pi} \ln \left(\frac{w_3}{1 - a^2}\right) \qquad (20)$$

where s is the riblet spacing. The result of this transformation can be seen in Fig. 19. The broken line is the stagnating streamline $\Psi = 0$ and is equivalent to the location of the wall with u = 0. The height of the riblets can be controlled by changing the radius a of the circle in the w_2-plane (see Fig. 19). After some intermediate calculations, one can find the relation which determines the riblet height h

$$h/s = \frac{1}{\pi} \operatorname{artanh} a \qquad (21)$$

with the above outlined procedure, a set of flow patterns has been calculated for various riblet heights, see Figs. 20 to 23.

The protrusion height h_p is the height of the riblet h minus the upwards shift of the streamlines (lines of constant u) in the w_4-plane of Fig. 19. Its magnitude can be determined by carefully tracking down the locations of the points in the different planes after the different transformations. We find after some intermediate calculations

$$\frac{h_p}{s} = \frac{1}{\pi} \ln \left[1 + \tanh \left(\frac{\pi h}{s}\right)\right] \quad . \qquad (22)$$

From eq. (22), one can see, that $h_p \approx h$ for small h/s. This means, that for very small blade riblets, the protrusion height is equal to the real height of the blade riblets.

On the other hand, for large blade heights, the blade riblets behave like the sawtooth riblets, see Fig. 18. This is due to the fact, that for very deep grooves only the top of the blade takes the viscous force. Obviously, the top of the blade is identical for deep grooves on sawtooth riblets and on blade riblets. Thus, the limit value for the protrusion height is again $h_p/s \to \ln 2/\pi$ for large h/s.

2.2.3. Scalloped riblets

Riblets with scalloped cross section are found on the scales of fast sharks. In laboratory experiments, it has been shown, that scalloped riblets with semicircular shape match the best sawtooth riblets with a drag reduction of 7-8% [4,23]. The viscous flow calculation on these scalloped riblets can be carried out with a modification of the transformations we had used for blade riblets.

The Kutta-Joukowsky transformation in the preceding section (eq. (18)) had a constant a being equal to the cylinder radius a. We obtain scalloped riblets if this radius of the mapping circle, which we call now b, is larger than the cylinder radius a, see Fig. 24. In addition, the mapping circle is no more coaxial with the cylinder. The position of the mapping circle has to be chosen so that it touches two streamlines with the same value (Ψ_c), but opposite sign, at the horizontal axis, $y_2 = 0$. The streamlines between $-\Psi_c$ and $+\Psi_c$ penetrate into the blade in the w_3 and w_4 planes. In the final plane w_4, the Ψ_c streamlines become the scalloped wall contour of the riblets. By numerical trial, cylinder radius and mapping circle radius can be adjusted so that the riblet contour is very close to a semi-circle. This particular configuration and its flow distribution is shown in Fig. 26. Of course, the velocity value on the surface has to be readjusted so that u = 0 at the contour Ψ_c. In this particular case, the protrusion height is $h_p/s = 0.192$ h/s. Other scalloped surfaces and their flow distributions are given in Figs. 25 and 27. In general, the protrusion height of scalloped riblets lies between sawtooth riblets and blade shaped riblets. But, as one can see from Fig. 18, they can be indeed very close to blade riblets. Of course, mechanically, scalloped riblets are much more durable than blade riblets.

2.2.4. Rounded ridges

There are several ways to calculate the viscous flow around rounded edges of riblet surfaces:

a) One can choose a line u = const above the actual surface of the sawtooth or blade shaped riblet and can consider this as the new surface. This produces a variety of riblet surfaces with rounded edges.

b) Similar to the preceding modification of the mapping function which produced scalloped riblets one can modify the Kutta-Joukowsky transformation into the other direction, which is more familiar from airfoil theory. If one choses a mapping circle radius smaller than the cylinder radius, one obtains "club"-like blade riblets with rounded edges, see Fig. 28. Also the modified flow pattern can be seen in the example calculated in Fig. 28.

From the numerical data of various "club"-like configurations, in particular for comparatively thin blades, we have compiled an approximate formula for the loss in protrusion height Δh_p, as compared to the thin blade riblets

$$\frac{\Delta h_p}{h_p} \approx \frac{2t}{s} \qquad (23)$$

where t is the maximum thickness of the blade. This approximate equation is valid for $t/s < 0.1$.

At the present time, however, we have not yet found a general law for the influence of the radius of curvature at the edge on the protrusion height. Nevertheless, we feel that this may be possible by an extension of the present analysis.

2.2.5. Convex riblets

Due to a programming error in our data plotting program for sawtooth riblets, we ran inadvertently into the solution of this problem. We change the mapping function for sawtooth riblets with n = 4, eq. (13), by omitting the second term:

$$w_3 = \frac{s}{2}\left(1+\frac{i}{\pi}\ln\frac{1+\xi}{1-\xi}\right);\ \text{with}\ \xi = \left(\frac{w_2-1}{w_2+1}\right)^{1/n}. \quad (24)$$

Instead of the originally expected pattern, we get the viscous flow above 2 convex riblets per division s. By varying the parameter $n = \pi/\alpha$ in the function ξ of eq. (24), we can vary the depth of the grooves. Fig. 29 and 30 show the viscous flow on convex riblets, calculated with the mapping function eq. (24), the grid size being normalized to obtain one riblet per division s.

The protrusion height can be calculated for each pattern. It is $h_{p/s} = 0.0724$ for Fig. 29 and $h_{p/s} = 0.0767$ for Fig. 30. For convex riblets, the protrusion height is always very small. This explains why experiments with convex riblet patterns have been unsuccessful in terms of drag reduction [23].

3. Considerations leading to three-dimensional riblets

The basic idea of the shear stress reduction of a turbulent boundary layer is to decrease the momentum exchange in the vicinity of the wall by impeding the streamwise vortices. We consider the protrusion height as the crucial quantity for the interaction with these vortices. On the other hand, in the preceding sections, a clear limit of the protrusion height has become visible, i.e., $(h_{p/s})_{max} = \ln 2/\pi = 0.2206$. For a suitable riblet spacing, we may assume, say, half the spacing of the natural streamwise vortices. This leads to $s^+ \approx 22$ (see Fig. 9). Thus, with the above mentioned limit for the protrusion height, we find $h_{p_{max}}^+ \approx 5$, in wall units. However, the cores of the streamwise vortices are much farther away from the surface. According to Fig. 7, the vortex cores are located at about $y^+ \approx 35$. Consequently, the interaction between two-dimensional riblets (of any conceivable shape) and the streamwise vortices remains indeed limited.

However, inventors do not give up that soon. There is still a possibility to increase the protrusion height far beyond $y^+ \approx 5$, which we are going to explain now. The streamwise vortices have a comparatively long wavelength in the downstream direction. Thus, it may be sufficient to have riblets with finite length in the downstream direction and, say, about 1-3 short riblets per longitudinal wavelength. A staggered array of riblets might then be suitable, see Fig. 31. A sharp swept leading edge should help to prevent secondary flows. Hence, short riblets with the shape of a section of a circle or of a swept fin look promising. In a staggered array, such as in Fig. 31, the lateral distance can be doubled and, therefore, also the protrusion height can be increased substantially. As we will see in the next section, the protrusion height of the point of highest elevation of short staggered riblets can be increased even beyond double the value of two-dimensional riblets.

Looking through our shark scale atlas [6] reveals readily, that we aren't the greatest inventors anyway [30]. For very fast sharks, we find intersecting and overlapping scales with staggered riblets quite often, or better say, almost everywhere. Indeed, the jagged trailing edge of the hand-like scales fits into the leading edge region of the consecutive scale like the two halves of a zipper, automatically producing an array of staggered riblets. Fig. 32 and 33 show photographs of such "zipper" structures on the skin of two different species of fast sharks.

However, the conditions under which shark skin samples are dried to be photographed, are not always ideal. There is no fluid shear force anymore to close the "zipper" during the drying process. Thus, not all available photographs of shark skin show actually interlocking scales.

4. Electrolytic experiments

It is desirable to have an independent proof for the 2-D riblet calculations and a simple and quick method to demonstrate the potential of 3-D staggered riblets to produce an increased protrusion height.

As before, the task is to solve the Laplace equation $\nabla^2 u = 0$ with our particular boundary conditions, i.e., $u = 0$ on the surface of the riblets. It is well-known that the electric field in a conductor, e.g., an electrolyt, obeys the same Laplace equation. In a model experiment, lines of constant velocity u would correpond to lines of constant voltage V in an electrolytic tank. However, besides tracking down velocity distributions by a point probe, we can also measure easily such quantities like the protrusion height. Mainly for this purpose we have established a measuring setup which is shown schematically in Fig. 34. We measure the resistance R of the rectangular electrolytic tank without and with riblet electrode via a voltage measurement (Fig. 34). The resistance of the tank without riblet electrode is proportional to the length L of the tank. The decrease in the resistance caused by the presence of the riblet electrode is equivalent to a decreased length L' of the electrolyt. We have

$$L - L' = h - h_p \quad (25)$$

and

$$h_p = h - (L - L'), \quad (26)$$

where h_p is the protrusion height and h is the geometrical height of the riblet, as before. The shape of the riblet electrode has to be chosen so that the walls of the rectangular tank are symmetry planes. The details of the experimental setup are given in appendix C.

The electrolytic measurements of the protrusion height h_p/s plotted versus the geometrical height h/s can be seen in Fig. 35. The agreement clearly shows, that our calculations are correct. There is, however, a systematic deviation: The measurements on the blade riblets show a protrusion height being about 5% lower than the theoretical values. We argue that this minor discrepancy is caused by the finite thickness of the blades of the blade riblet electrodes. The blade thickness is $t = 0.025$ s. Then our approximate formula for the decrease of the protrusion height, eq. (23) would predict a decrease of 5%. Thus, the discrepancy is explained.

For our 3-D demonstration electrode, we have chosen the dimensions which can be seen in Fig. 36. The protrusion height which we found experimentally is $h_p = 0.55$ s. This is more than twice the protrusion height of a comparable 2-D riblet.

Acknowledgement

The authors would like to thank Dr. A. Dinkelacker, Max-Planck-Institut für Strömungsforschung, Göttingen, for the stimulating discussions. Funding for the biological studies was provided by the Deutsche Forschungsgemeinschaft (DFG), Sonderforschungsbereich 53.

References

1. Kramer, M.O.: "Boundary layer stabilization by discributed damping". JAS 27, 69 (1960); see also: JAS 24, 459-460 (1957).

2. Carpenter, P.W., Gaster, M., Morris, P.: "Optimization of compliant surfaces for transition delay". Paper presented at the "Drag reduction and boundary layer control symposium" National Academy of Sciences, Washington, D.C., 22-25, October 1985.

3. Hoyt, J.W.: "Hydrodynamic drag reduction due to fish slimes" in " Swimming and flying in nature" Vol. 2, Ed.: Y.-T. Wu,C.J. Brokaw, C. Brennen. New York: Plenum Press, 1975.

4. Bechert, D.W., Hoppe, G., Reif, W.-E.: "On the drag reduction of the shark skin". AIAA-Paper 85-0546 (1985).

5. Bone, Q.: "Muscular and energetic aspects of fish swimming" in "Swimming and flying in nature" Vol. 2., Ed.: Y.-T. Wu, C.J. Brokaw, C. Brennen. New York: Plenum Press, 1975.

6. Reif, W.-E.: "Squamation and Ecology of sharks". Courier Forschungsinstitut Senckenberg, Frankfurt/M., FRG (1986). Bd. Nr. 78; 255 p.

7. Reif, W.-E., Dinkelacker, A.: "Hydrodynamics of the squamation in fast swimming sharks". Neues Jahrbuch fuer Geologie und Palaeontologie. Abhandlungen Band 164, pp. 184-187, Stuttgart: E. Schweizerbart'sche Verlagsbuchhandlung, 1982.

8. Reif, W.-E.: "Morphogenesis and function of the squamation in sharks". Neues Jahrbuch fuer Geologie und Palaeontologie. Abhandlungen Band 164, pp. 172-183, Stuttgart: E. Schweizerbart'sche Verlagsbuchhandlung, 1982.

9. Reif, W.-E.: "Biophysik und Morphologie schneller Schwimmer". Palaeontologische Kursbuecher, Band 1, Hrsg.: W.-E. Reif, Palaeontologische Gesellschaft, München 1981.

10. Steuben, K.S., Krefft, G.: "Die Haie der sieben Meere". Hamburg: Verlag Paul Parey, 1978.

11. Castro, J.I.: "The sharks of North American waters". College Station, Texas: Texas A&M University Press, 1983.

12. Wainwright, S.A., Vosburgh, F., Hebrank, J.H.: "Shark skin: Function in locomation". SCIENCE, Vol. 202, 17. Nov. 1978, pp. 747-749.

13. Bechert, D.W.: "Zur Vermeidung von Strömungsablösungen ausgebildete Oberfläche eines umströmten Körpers". Deutsche Patentanmeldung P 35 34 268.4 (1985).

14. Coles, D.: "A model for flow in the viscous sublayer". In: Proc. of: "Coherent structures of turbulent boundary layers", AFOSR/Lehigh Workshop 1978, pp. 462-475.

15. Van Dyke, M.: "An album of fluid motion" (ref. p. 93). Stanford, Cal.: The Parabolic Press, 1982.

16. Kline, S.J., Reynolds, W.C., Schraub, F.A., Runstadler, P.W.: "The structure of turbulent boundary layers". J. Fluid Mech. 30 (1967), pp. 741-773.

17. Smith, C.R., Metzler, S.P.: "The characteristics of low-speed streaks in the near-wall region of a turbulent boundary layer". J. Fluid Mech. 129 (1983), pp. 27-54.

18. Landahl, M.T.: "Wave breakdown and turbulence" J. Appl. Math. (1977), pp. 215-236.

19. Jang, P.S., Benney, D.J., Chen, Y.M.: "Origin of streamwise vortices in turbulent boundary layers". Bull. Am. Phys. Soc., Ser. II, Vol. 29, No. 9, Nov. 1984, Paper BB8, p. 1528. See also: "On the origin of streamwise vortices in a turbulent boundary layer" by P.S. Jang, D.J. Benney & R.L. Gran, Dynamics Technology, Inc., 21311 Hawthorne Blvd., Suite 300, Torrance, Cal., 90503, Report March 1985.

20. Morrison, W.R.B., Bullock, K.J.,, Kronauer, R.E.: "Experimental evidence of waves in the sublayer". J. Fluid Mech. 47 (1971), pp. 639-656.

21. Hooshmand, D., Youngs, R., Wallace, J.M.: "An experimental study of changes in the structure of a turbulent boundary layer due to surface geometry changes". AIAA-paper 83-0230 (1983).

22. Walsh, M.J.: "Drag characteristics of V-groove and transverse curvature riblets" in "Viscous flow drag reduction" Ed.: G.R. Hough, Vol. 72 of Progress in Astronautics an d Aeronautics. New York: American Institute of Aeronautics and Astronautics, 1980.

23. Walsh, M.J.: "Turbulent boundary layer drag reduction using riblets". AIAA-paper 82-0169 (1982).

24. Serafini, J.S.: "Wall-pressure fluctuations and pressure-velocity correlations in a turbulent boundary layer". Paper presented at the AGARD meeting on "The mechanism of noise generation in turbulent flow", April 1-4, 1963, Brussels, Belgium.

25. Betz, A.: "Konforme Abbildung", Berlin: Springer-Verlag, 1964.

26. Kober, H.: "Dictionary of conformal representations". New York: Dover Publications, 1957.

27. Gradstein, I.S., Ryshik, I.M.: "Tables of series, products, and integrals". (Transl. from Russian) Frankfurt/ M.: Verlag Harri Deutsch, 1981.

28. Abramovitz, M., Stegun, I.A.: "Handbook of mathematical functions". New York: Dover Publications, 1972.

29. Wilkinson, S.P.: "Turbulent flows measurements over a flat plate with various near wall flow-aligned elements". Paper presented at the "Drag reduction and boundary layer control symposium". National Academy of Sciences, Washington, D.C., 22-25 October 1985.

30. Bechert, D.W.: "Verminderten Stroemungswiderstand durch herabgesetzte Wandschubspannung aufweisende Oberflaeche eines turbulent ueberstroemten Koerpers". Deutsche Patent-Anmeldung, 21. Maerz 1986.

Appendix A

Transformation functions for various angles of sawtooth riblets.

Note: In all cases we have $w_2 = \sin w_1$

and $\xi = \left(\frac{w_2-1}{w_2+1}\right)^{1/n}$.

1.) Normalized undistorted grid $n = 2$; $\alpha = 90^\circ$

$$w_3 = \frac{s}{2}\left[1 + \frac{i}{\pi} \ln \frac{1+\xi}{1-\xi}\right] = \frac{s}{2\pi}\left(w_1 + \frac{\pi}{2}\right) \qquad (A1)$$

2.) $n = 3$; $\alpha = 60^\circ$; ridge angle: 120°

$$w_3 = \frac{s}{2}\left[1 + \frac{i}{\pi}\left(\ln \frac{\sqrt{1+\xi+\xi^2}}{1-\xi} + \sqrt{3} \arctan \frac{2\xi+1}{\sqrt{3}} - \sqrt{3} \arctan \frac{1}{\sqrt{3}}\right)\right] \qquad (A2)$$

3.) $n = 4$; $\alpha = 45^\circ$; ridge angle: 90°

$$w_3 = \frac{s}{2}\left[1 + \frac{i}{\pi}\left(\ln \frac{1+\xi}{1-\xi} + 2 \arctan \xi\right)\right] \qquad (A3)$$

4.) $n = 6$; $\alpha = 30^\circ$; ridge angle: 60°

$$w_3 = \frac{s}{2}\left[1 + \frac{i}{\pi}\left(\ln \frac{1+\xi}{1-\xi} - \frac{1}{2} \ln \frac{\xi^2-\xi+1}{\xi^2+\xi+1} + \sqrt{3} \arctan \frac{2\xi-1}{\sqrt{3}} + \sqrt{3} \arctan \frac{2\xi+1}{\sqrt{3}}\right)\right] \qquad (A4)$$

5.) $n = 8$; $\alpha = 22.5^\circ$; ridge angle: 45°

$$w_3 = \frac{s}{2}\left[1 + \frac{i}{\pi}\left(\ln \frac{1+\xi}{1-\xi} - \frac{1}{\sqrt{2}} \ln \frac{\xi^2-\sqrt{2}\xi+1}{\xi^2+\sqrt{2}\xi+1} + 2\arctan \xi + \sqrt{2} \arctan (\sqrt{2}\xi-1) + \sqrt{2} \arctan (\sqrt{2}\xi+1)\right)\right]. \qquad (A5)$$

Appendix B:

The protrusion height of sawtooth shaped riblets.

The aim of this section is to find a general equation for the protrusion height of sawtooth riblets with arbitrary angle. To achieve this we have to track down where the points of the grid move if the conformal transformations are carried out. We focus on points farther away from the surface with large y_1 in the w_1-plane. We have for w_2

$$w_2 = \sin w_1 = \sin (z_1+iy_1) = \sin z_1 \cosh y_1 + i \cos z_1 \sinh y_1. \qquad (B1)$$

In particular for $z_1 = \pi/2$ (see Fig. 13) we obtain $w_2 = \cosh y_1$. For large y_1 this becomes $\approx e^{y_1}/2$. For the transformation from the w_2 plane to the w_3 plane we use a variable ξ_n*)

$$\xi_n = \left(\frac{w-1}{w+1}\right)^{\frac{1}{n}} \qquad (B2)$$

This variable becomes then for large y_1

$$\xi_n \approx 1 - \frac{4}{n} e^{-y_1} \quad \text{or:} \quad \xi_n \to 1 \text{ for } y_1 \to \infty . \qquad (B3)$$

The transformation function (eq. (11)), with appropriately determined constants assumes the form

$$w_3 = \frac{s}{2} + \frac{isn}{2\pi} \int_0^{\xi_n} \frac{d\xi}{1-\xi^n} \qquad (B4)$$

As we see from Fig. 13, the shift d between the reference grid ($n = 2$) and the riblet surface grid ($n = \pi/\alpha$) is a quantity from which we can calculate the protrusion height. We have for large y_3

$$d = y_3(n = \tfrac{\pi}{\alpha}) - y_3(n = 2), \qquad (B5)$$

and

$$h_p = h - d = \frac{s}{2} \cdot \operatorname{cotg} \alpha - d ; \qquad (B6)$$

we omitted here the i-coefficient. Using eq. (B4) we have

$$d = \frac{s}{2\pi} \lim_{y_1 \to \infty} \left[n \int_0^{\xi_n} \frac{d\xi}{1-\xi^n} - 2 \int_0^{\xi_2} \frac{d\xi}{1-\xi^2}\right] \qquad (B7)$$

where the index 2 in ξ_2 stands for $n = 2$, referring to the reference grid on the right hand side of Fig. 13. We change again the integration variable in the integrals by putting $\xi^n = \kappa$. We obtain

$$n \int_0^{\xi_n} \frac{d\xi}{1-\xi^n} = \int_0^{\frac{w-1}{w+1}} \frac{\frac{1}{n}}{\kappa^n} \frac{d\kappa}{\kappa(1-\kappa)} \qquad (B8)$$

The difference of the two integrals in brackets of e.q. (B7) can then be expressed, using eq. (B3):

$$I = \int_0^1 \frac{\kappa^{\frac{\alpha}{\pi}} - \kappa^{\frac{1}{2}}}{\kappa(1-\kappa)} \quad \text{for} \quad 0 < \alpha < \pi/2 \qquad (B9)$$

This integral we could not find in integral tables [27]. Nevertheless, we managed to find a way to perform the integration analytically. The problem is, that the integral I cannot be split into two parts, because the two constituents of the integral I do not converge by themselves. However, by introducing a convergence coefficient ε, which we eliminate finally, we can split the integral

$$I = I_1 + I_2$$

$$I_1 = \int_0^1 \kappa^{\frac{\alpha}{\pi} - 1} (1-\kappa)^{\varepsilon-1} \, d\kappa \qquad (B10)$$

$$I_2 = \int_0^1 \kappa^{-\frac{1}{2}} (1-\kappa)^{\varepsilon-1} \, d\kappa$$

The integrals I_1 and I_2 are Beta functions [27].

$$I_1 = B(\tfrac{\alpha}{\pi}, \varepsilon) \quad ; \quad I_2 = B(\tfrac{1}{2}, \varepsilon) \qquad (B11)$$

The Beta functions can be expressed in terms of Gamma functions [27]

$$I_1 = \frac{\Gamma\left(\frac{\alpha}{\pi}\right) \cdot \Gamma(\varepsilon)}{\Gamma\left(\frac{\alpha}{\pi} + \varepsilon\right)} ; \quad I_2 = \frac{\Gamma\left(\frac{1}{2}\right) \cdot \Gamma(\varepsilon)}{\Gamma\left(\frac{1}{2} + \varepsilon\right)} \qquad (B12)$$

Inserted in I and expanded for small ε gives

$$I = \frac{1}{\varepsilon}\left[\frac{1}{1 + \varepsilon \frac{\Gamma'\left(\frac{\alpha}{\pi}\right)}{\Gamma\left(\frac{\alpha}{\pi}\right)}} - \frac{1}{1 + \varepsilon \frac{\Gamma'\left(\frac{1}{2}\right)}{\Gamma\left(\frac{1}{2}\right)}}\right] \qquad (B13)$$

According to Abramovitz & Stegun [28], the ratio Γ'/Γ is defined as the Digamma function ψ. We find for small ε

$$I = \psi\left(\tfrac{1}{2}\right) - \psi\left(\tfrac{\alpha}{\pi}\right) \qquad (B14)$$

The value of $\psi\left(\frac{1}{2}\right)$ is

$$\psi\left(\tfrac{1}{2}\right) = -(\gamma + 2 \ln 2) \qquad (B15)$$

where γ is the Euler constant $\gamma = 0.5772$. Using equations (B6) and (B7) we find for the protrusion height h_p

*) For clarity, we introduce here the subscript n.

$$\frac{h_p}{s} = \frac{\cot g\ \alpha}{2} + \frac{1}{2\pi}\left[\gamma + 2\ \ln\ 2 + \psi(\frac{\alpha}{\pi})\right] \qquad (B16)$$

Since the tables for ψ [28] are available only for arguments exceeding the value 1, we rewrite this formula with the recurrence relation [28]

$$\psi(z) = \psi_{(z+1)} - \frac{1}{z} \qquad (B17)$$

Thus, we have finally the general formula for the protrusion height of sawtooth riblets

$$\frac{h_p}{s} = \frac{\cot g\ \alpha}{2} + \frac{1}{2\pi}\left[\gamma + 2\ \ln\ 2 - \frac{\pi}{\alpha} + \psi(1+\frac{\alpha}{\pi})\right] \qquad (B18)$$

It can be shown by expanding this equation and using the tables of Abramovitz & Stegun [28] for specific values of special functions, that the saturation value for large heights (or small α) is

$$\left.\frac{h_p}{s}\right|_{\alpha \to 0} = \frac{\ln\ 2}{\pi}$$

for small riblet heights (or α close to $\pi/2$), on the other hand, the protrusion height is <u>half</u> the riblet height.

<u>Appendix C</u>

Description of the electrolytic experiments. Fig. 37 shows a photograph of our electrolytic simulation experiment. In the center, we see a Brüel & Kjaer type 1022 beat frequency generator as the A.C. source. On the right hand side, a digital voltmeter (Schlumberger 1240) is visible, and besides it, the reference 1KΩ resistor. On the left hand side, we have lined up a set of 2-D copper electrodes. By intermediate copper pieces, also visible on the left, the overall distance of the electrodes can be adjusted to the particular size of the riblet model electrodes. Several details of the experiment should be also mentioned:

a) The experiments can be carried out with A.C. only. A.C. does not lead to a buildup of gas layers at the electrodes, which would produce a very high resistance. The frequency should be as high as the digital voltmeter for the resistance measurement can take it. Of course, there is a limit by the skin effect at very high frequencies. We have taken our measurements at a frequency of 10 KHz.

b) We selected a non-poisonous electrolytic liquid in order to simplify the handling of the liquid. We used destilled water with a few percent of dish washer cleaning fluid, which consists of lemon acid and a detergent. A typical specific resistance is 100 Ω per cm length for a cross section of 10 cm^2. This led to values of the resistance in our tank in the order of 1 KΩ. Thus, the resistance of the electrodes and the wiring was negligible.

c) The tank was milled precisely. Deviations of fractions of a millimeter in the dimensions would lead to significant errors. The tank has a small ventilation tube and a funnel combined with an additional fluid reservoir. Bubbles were removed completely.

d) All electrodes were sanded and cleaned carefully before each test series. Reference resistance measurements of the tank without riblet electrode were taken before and after each measurement.

Figures

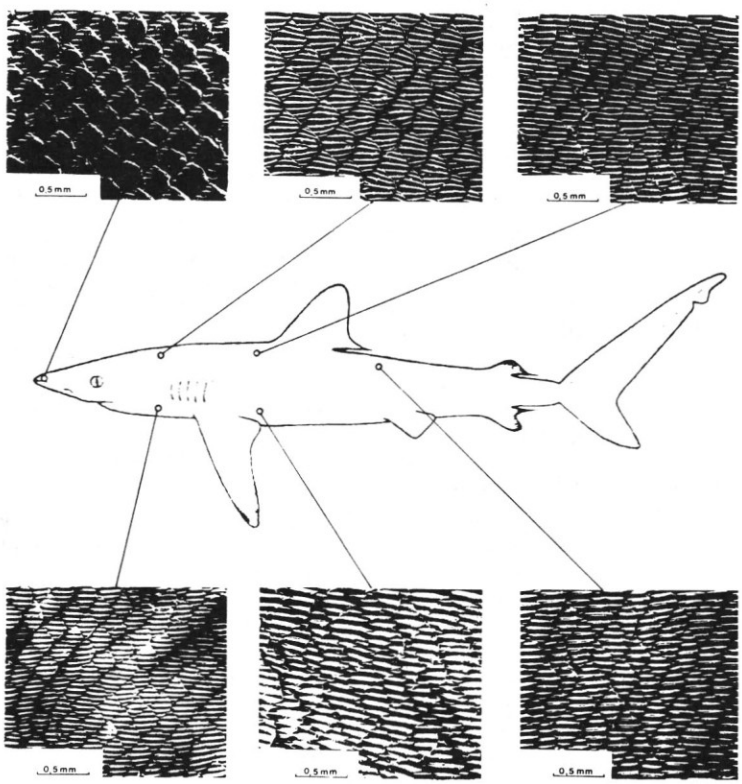

Fig. 1: SILKY SHARK, *Carcharhinus falciformis*, 2.27 m length.

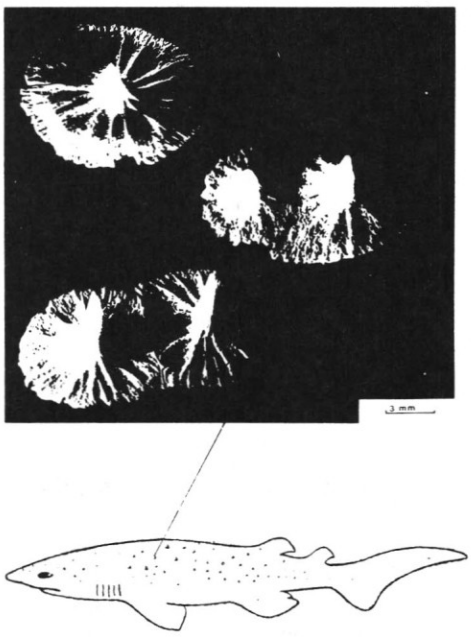

Fig. 2: BRAMBLE SHARK, *Echinorhinus brucus*, 1.90 m length.

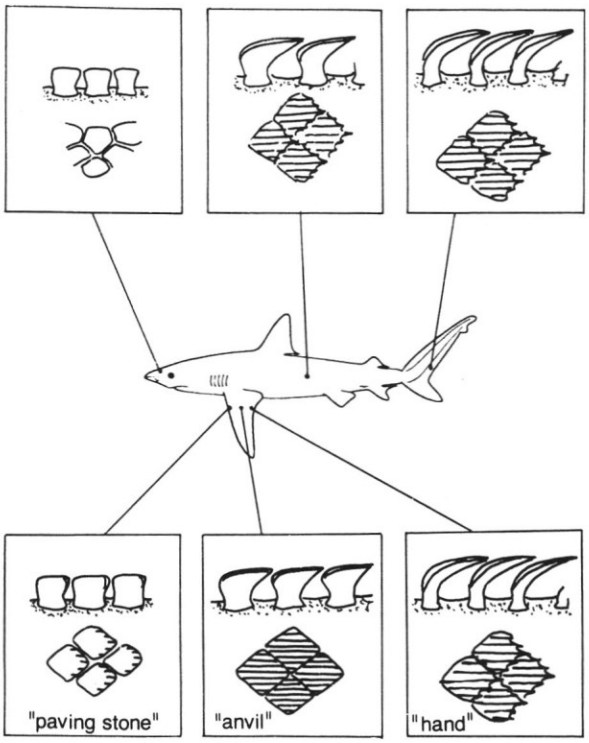

Fig. 3: GALAPAGOS SHARK, *Carcharhinus Galapagensis*, 2.55 m length, scale shapes on various locations of the body.

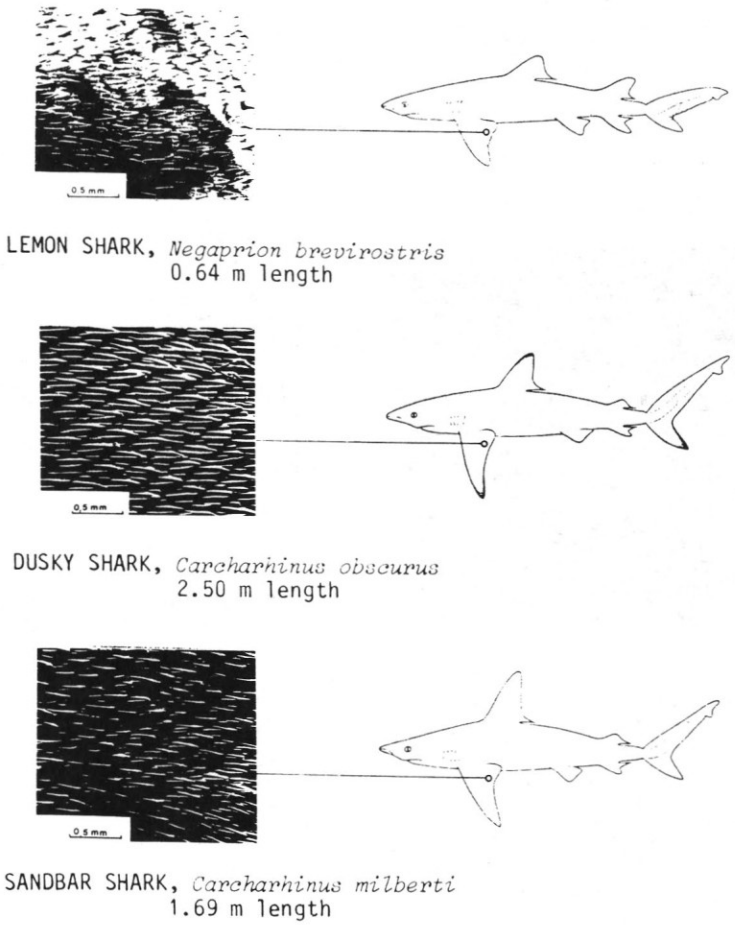

Fig. 4: V-shaped central ridge on scales of pectoral fins.

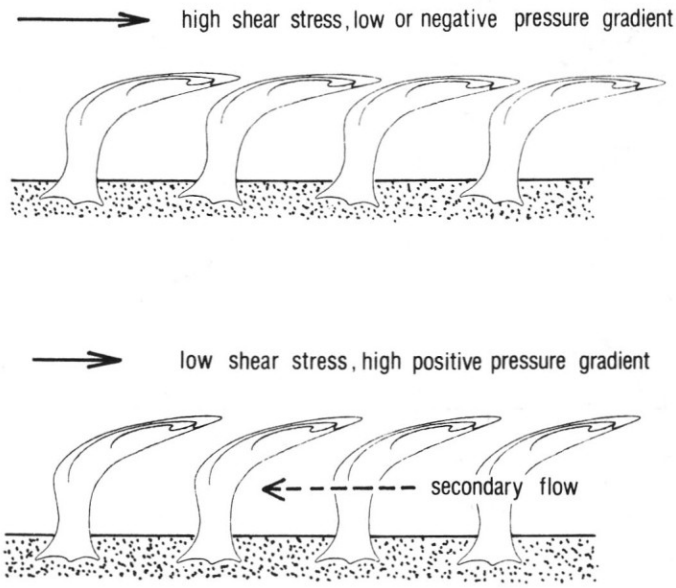

Fig. 5: Loosely suspended hand-like scales, controlled by a secondary flow underneath the surface.

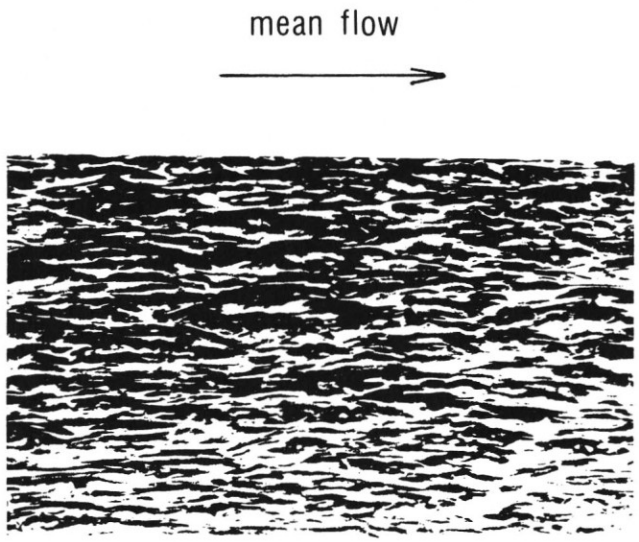

Fig. 6: Viscous sublayer flow structure as seen through a transparent wall, photograph by Cantwell, after Coles [14].

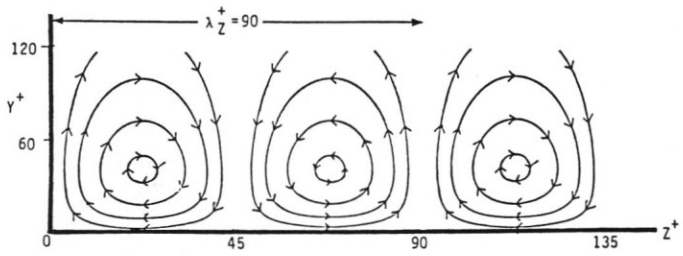

Fig. 7: Computed streamline pattern of the streamwise vortices, according to Jang et al. [19].

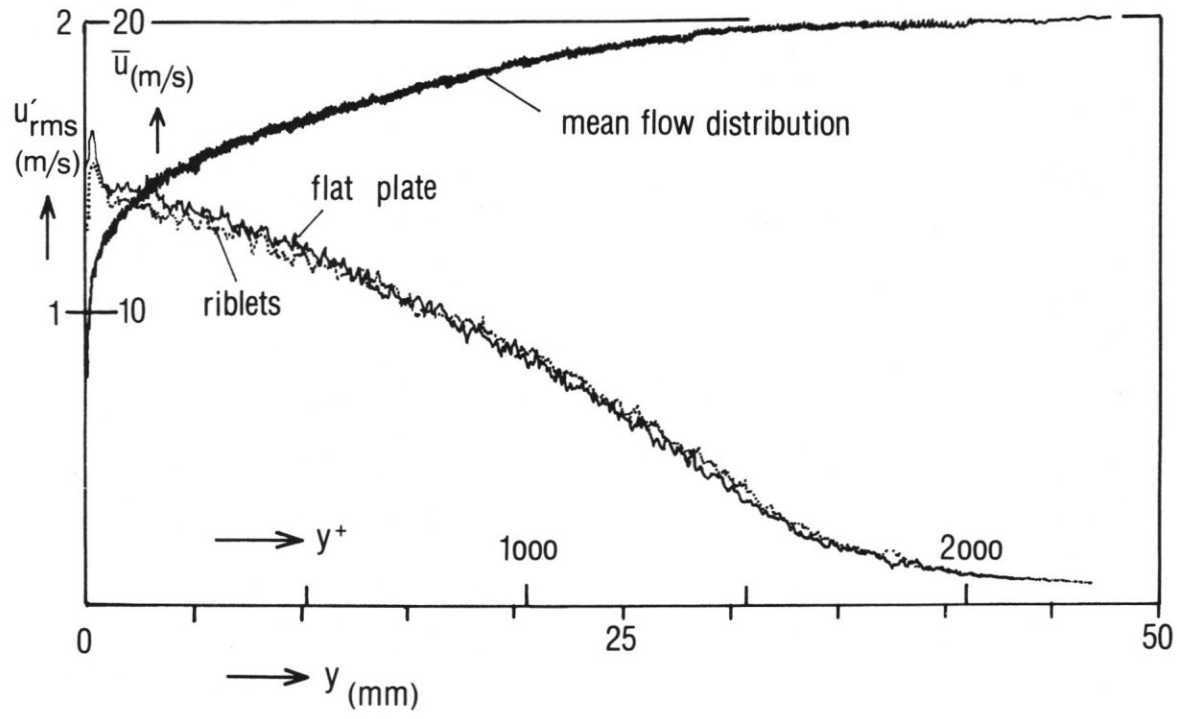

Fig. 8: Hot wire measurements of mean flow profile and velocity fluctuations u'_{RMS} for smooth and riblet surfaces.

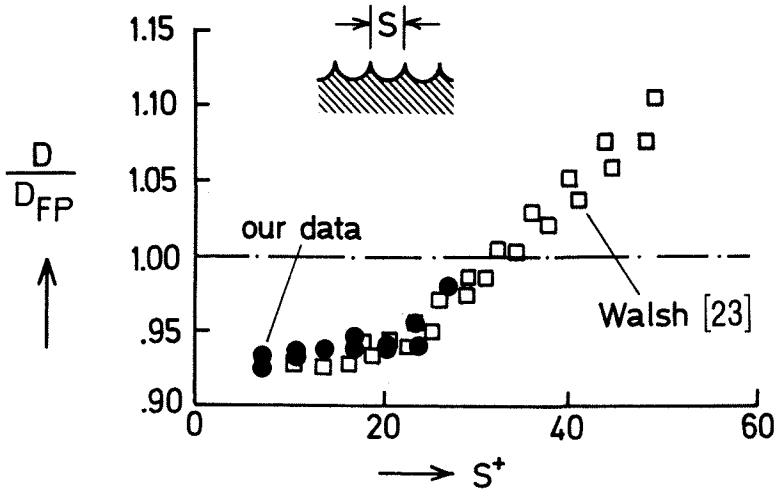

Fig. 9: Turbulent shear stress reduction by a riblet surface with scalloped cross section.

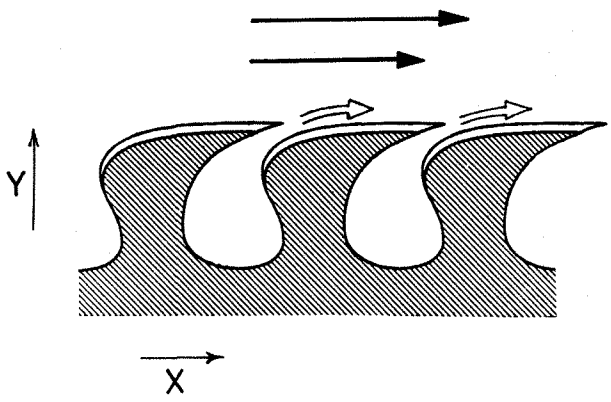

Fig. 10: Longitudinal cross section of a surface with slits for low speed streak cancellation by instantaneous streamwise fluid ejection.

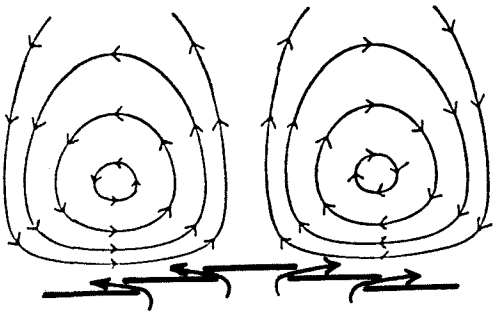

Fig. 11: Lateral blowing for low speed streak cancellation.

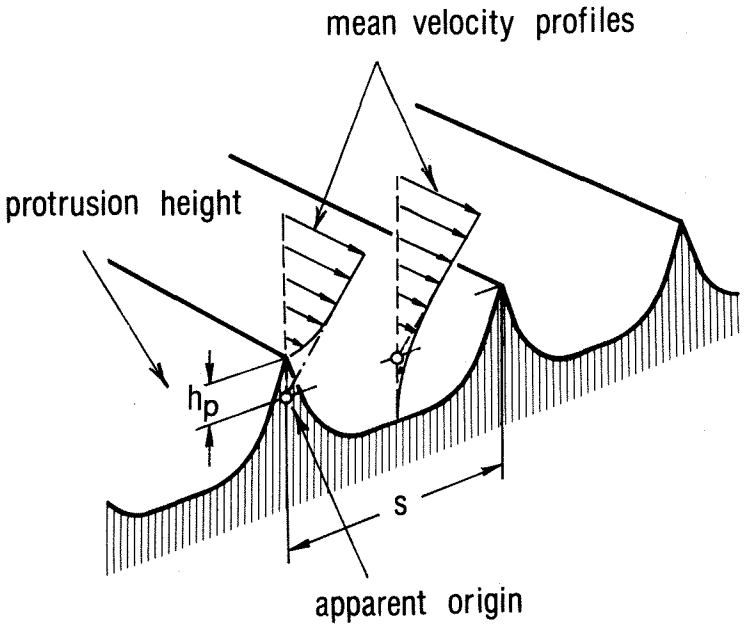

Fig. 12: Apparent origin of a riblet surface.

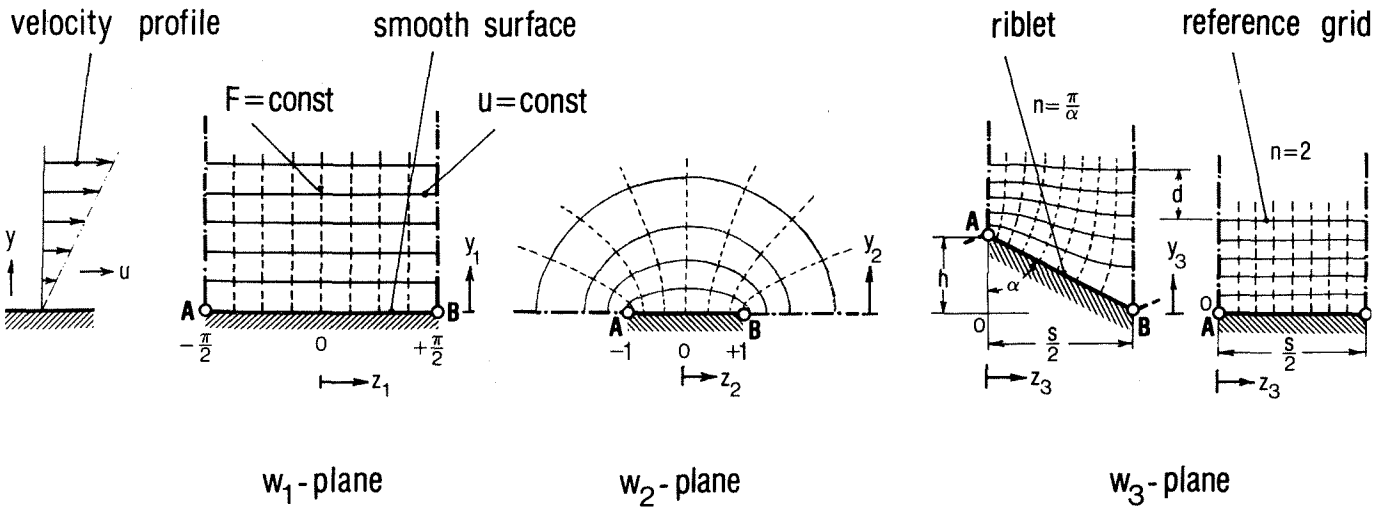

Fig. 13: Conformal transformations leading to the viscous flow on a sawtooth riblet surface.

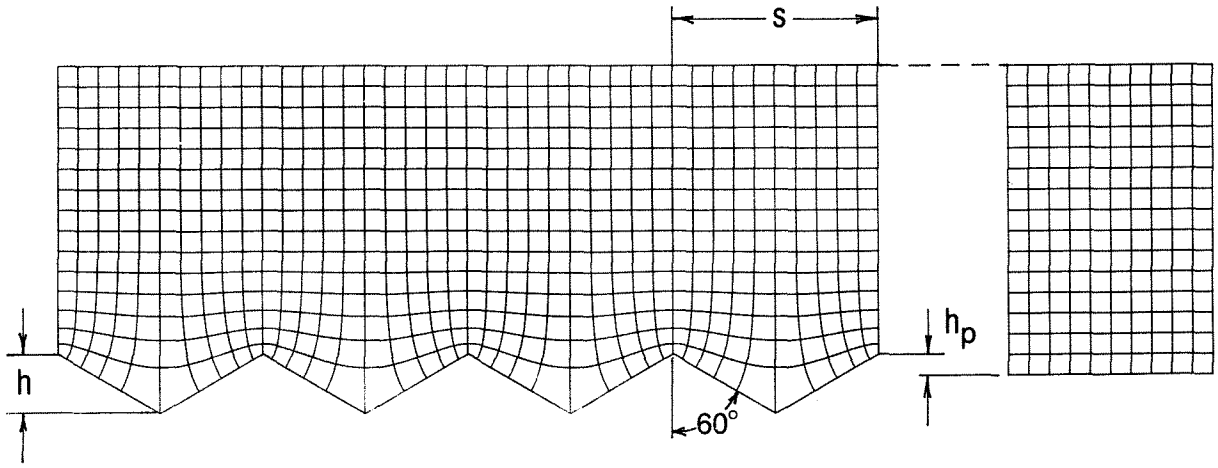

Fig. 14: u-velocity and fluid shear force distribution of the viscous flow on a sawtooth riblet surface. Riblet half-angle α = 60°.

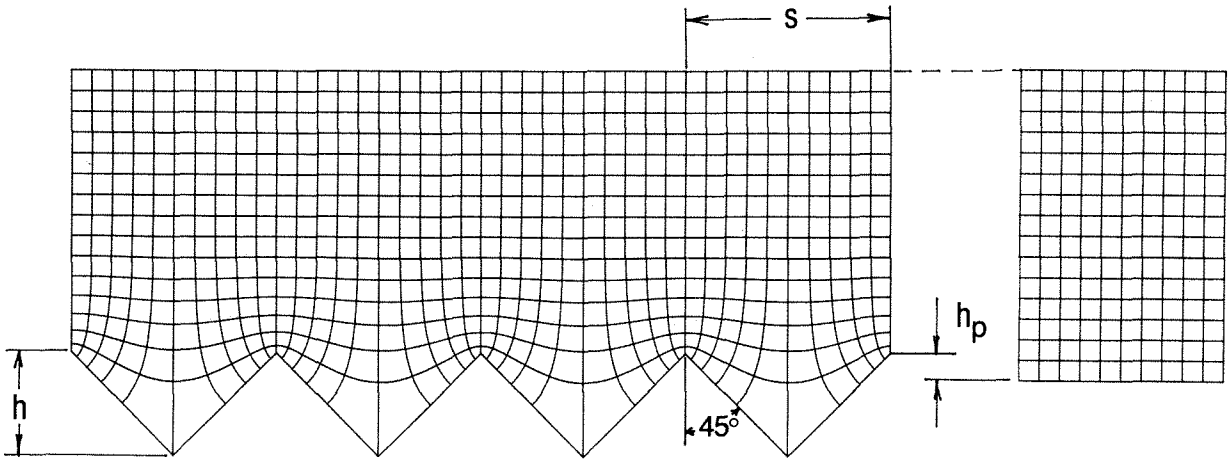

Fig. 15: Sawtooth riblet, half-angle 45°.

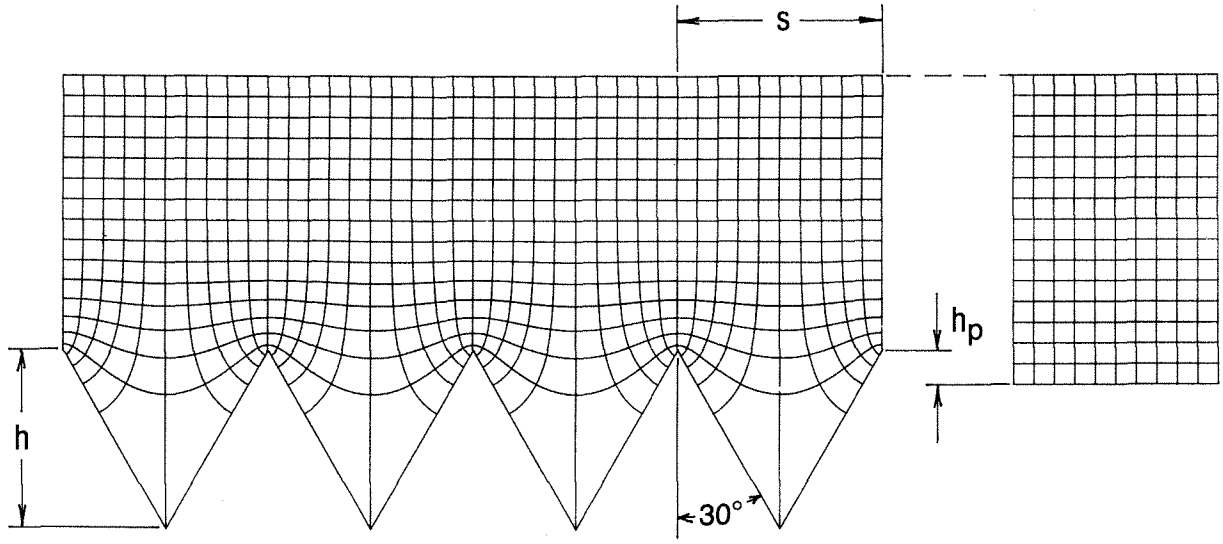

Fig. 16: Sawtooth riblet, half-angle 30°.

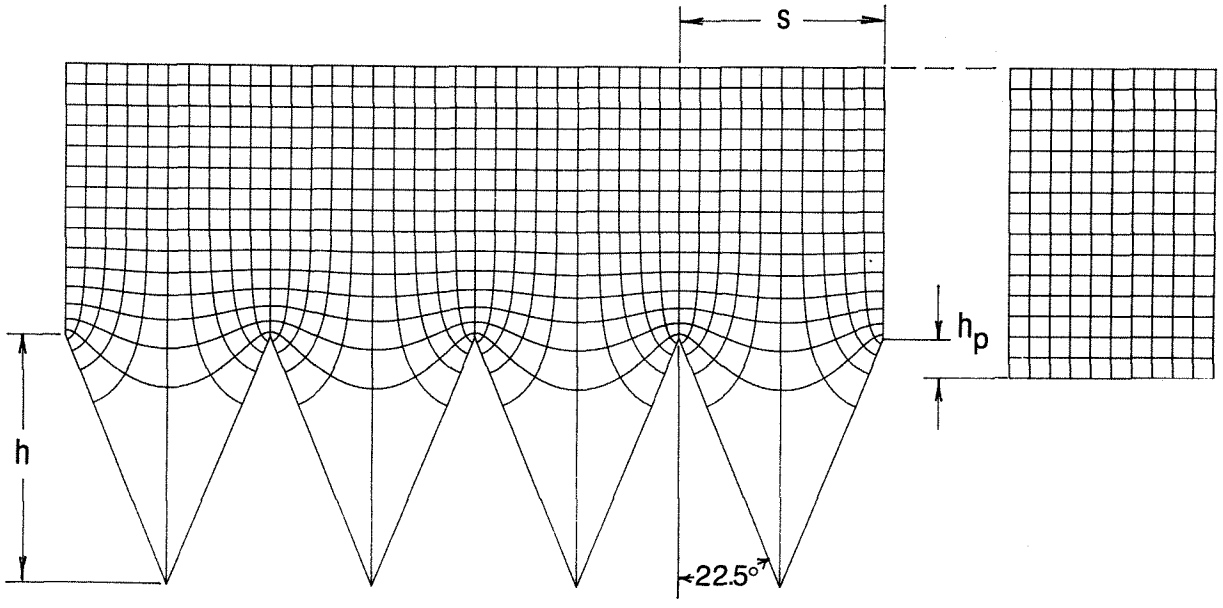

Fig. 17: Sawtooth riblet, half-angle 22.5°.

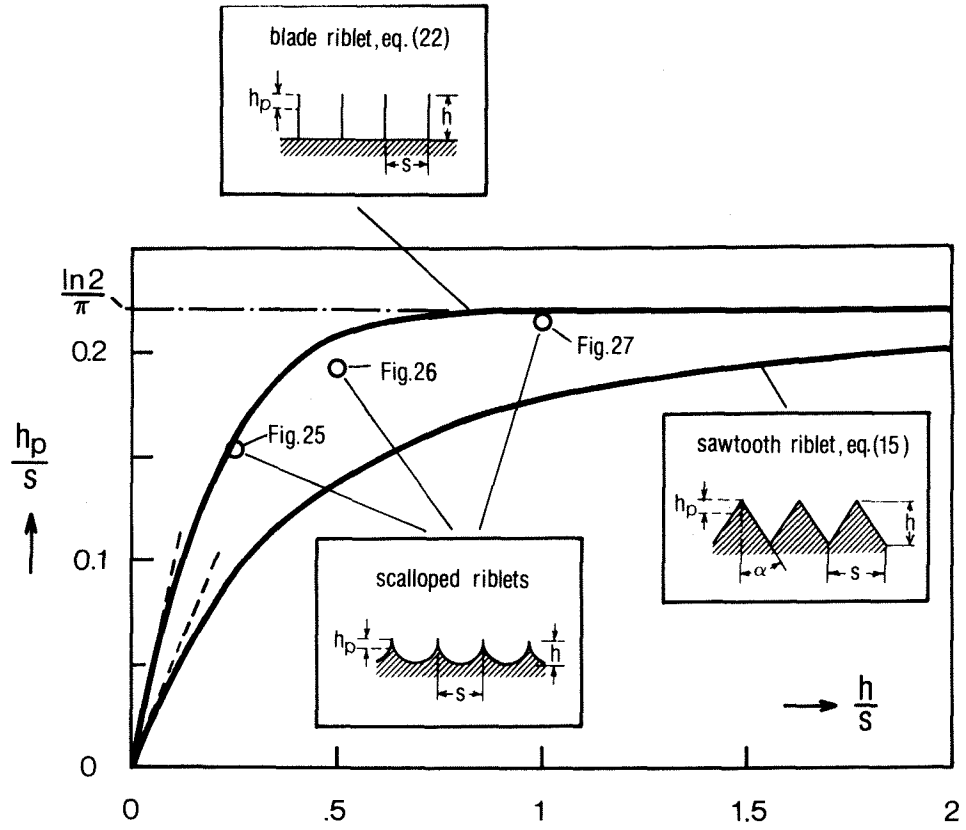

Fig. 18: Protrusion height as a function of geometrical height for different types of riblets.

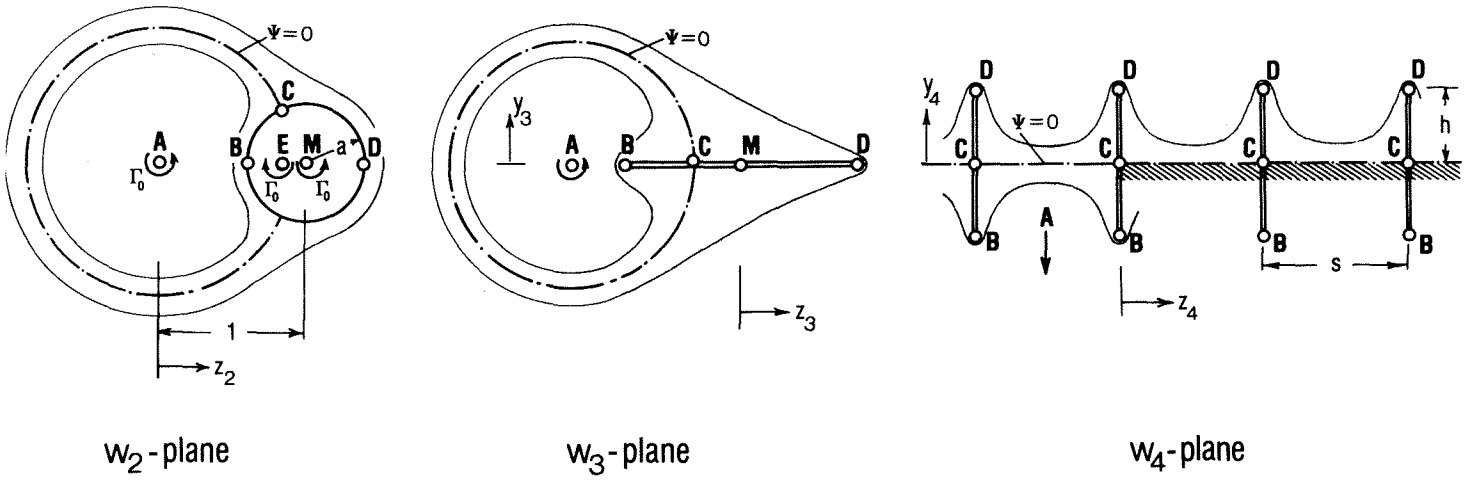

Fig. 19: Conformal transformations leading to the viscous flow on a blade riblet surface.

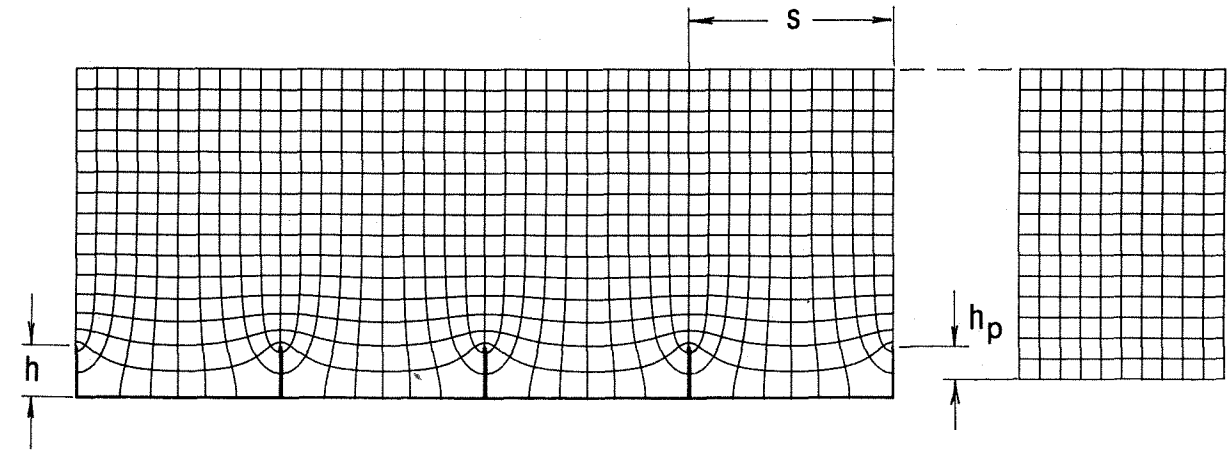

Fig. 20: u-velocity and fluid shear force distribution of the viscous flow on a blade riblet surface. Blade height h/s = 0.25.

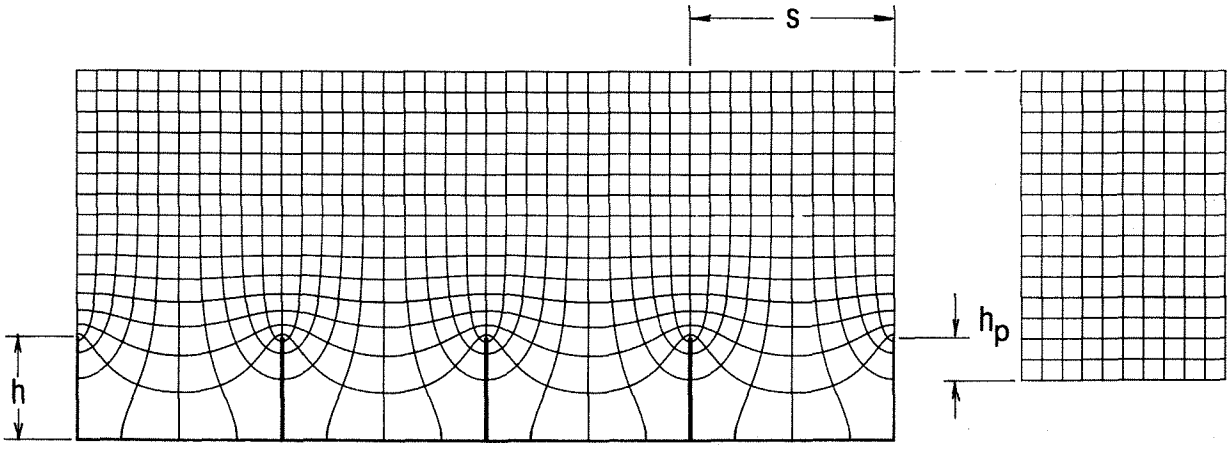

Fig. 21: Blade riblet, height h/s = 0.5.

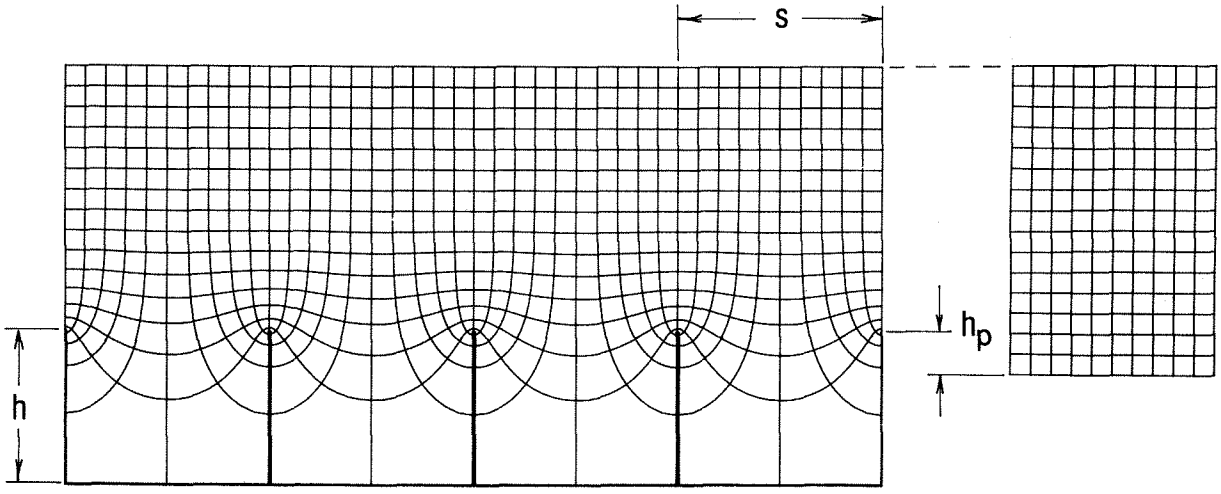

Fig. 22: Blade riblet, height h/s = 0.75.

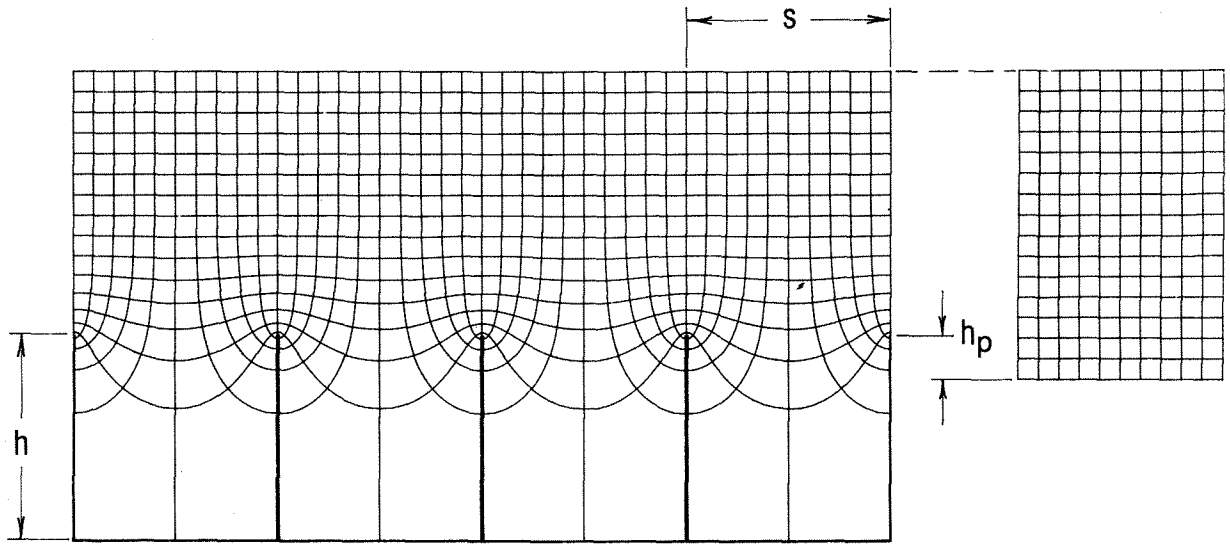

Fig. 23: Blade riblet, height h/s = 1.0.

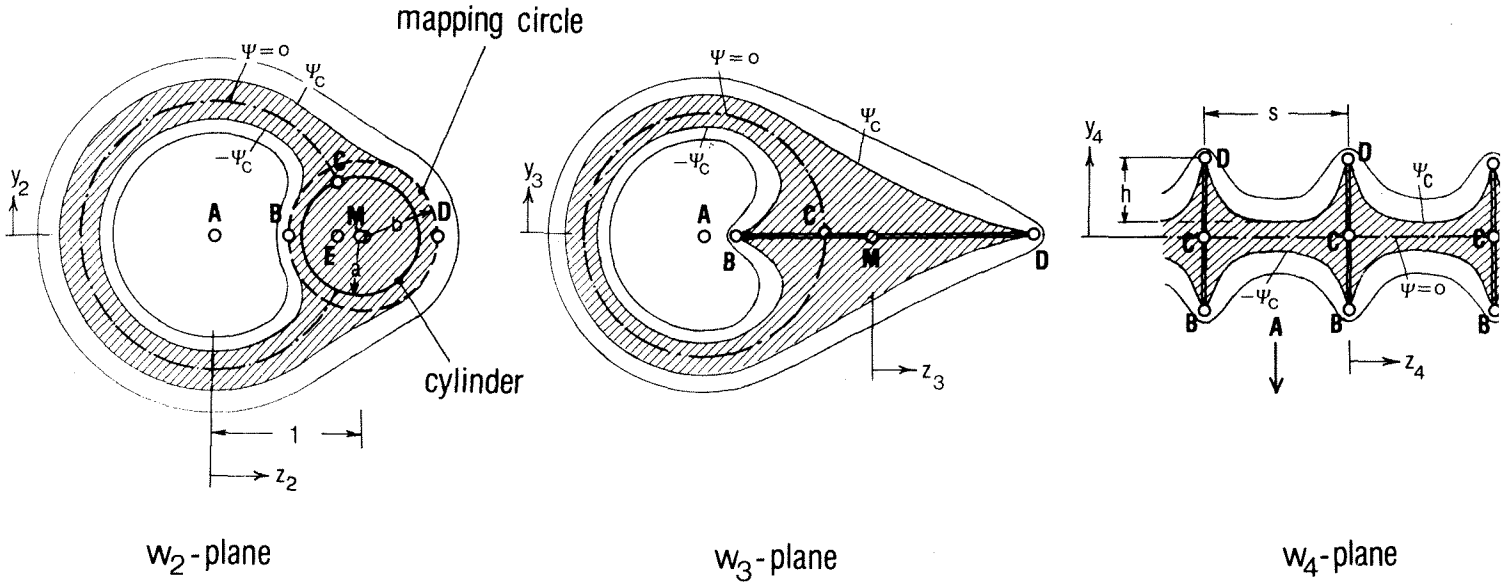

Fig. 24: Conformal transformations leading to the viscous flow on a riblet surface with scalloped cross section.

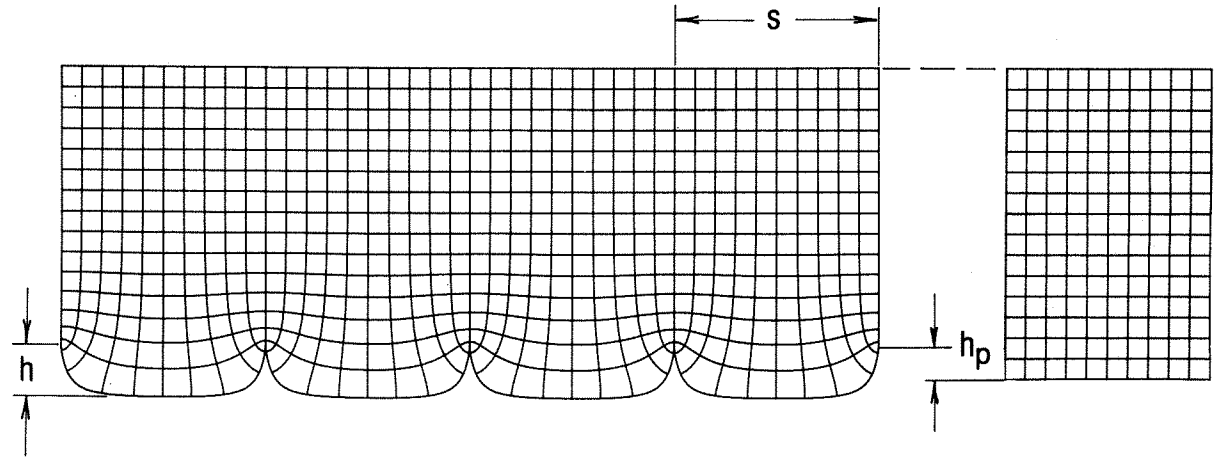

Fig. 25: u-velocity and fluid shear distribution of the viscous flow on a scalloped riblet surface. Riblet height h/s = 0.25, parameter a/b = 1.155, protrusion height h_p/s = 0.155.

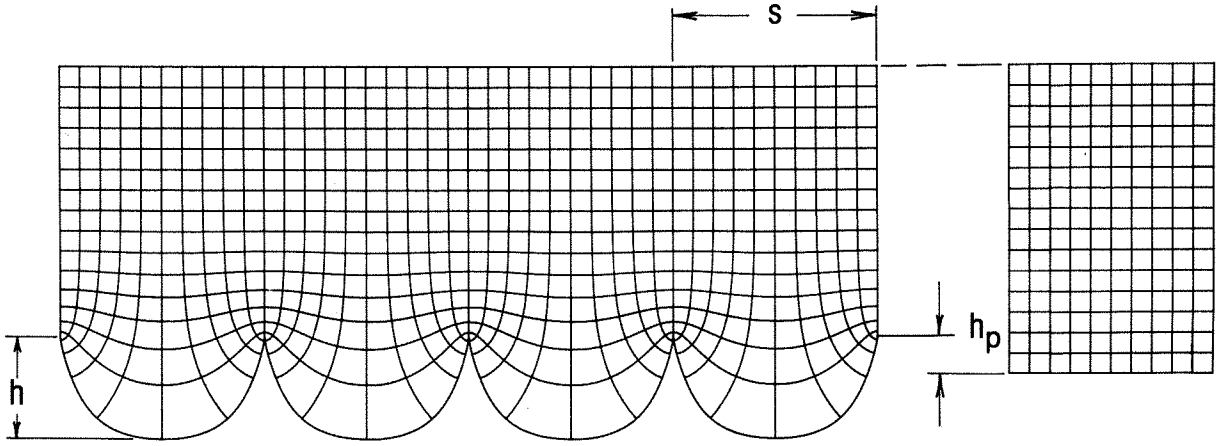

Fig. 26: Scalloped riblet with nearly semi-circular cross section. Riblet height h/s = 0.50, parameter a/b = 1.192, protrusion height h_p/s = 0.192.

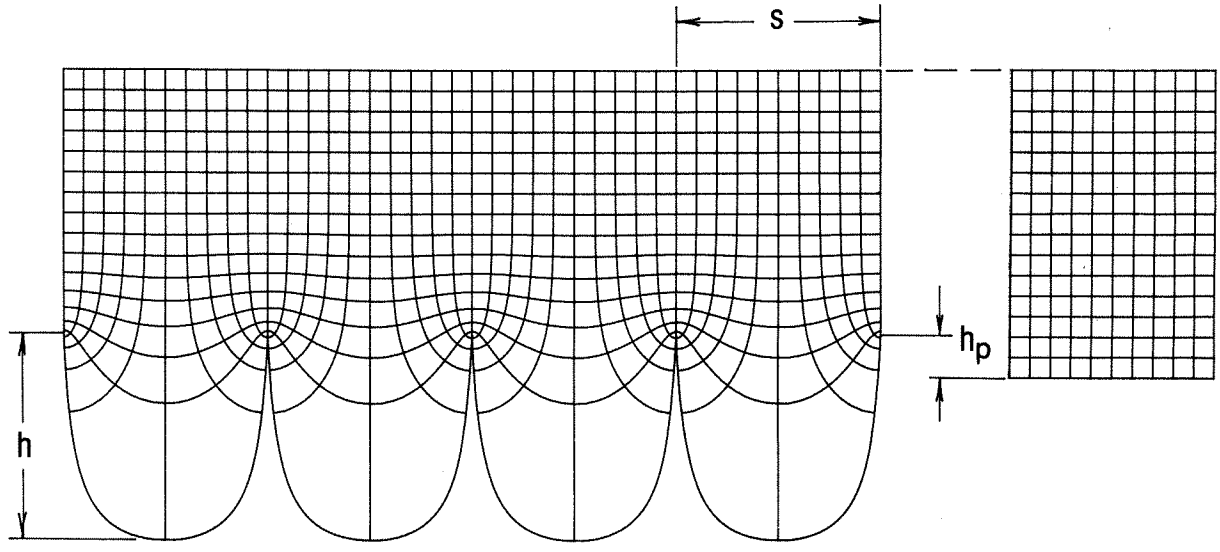

Fig. 27: Scalloped riblet; height h/s = 1.00, parameter a/b = 1.0325, protrusion height h_p/s = 0.216.

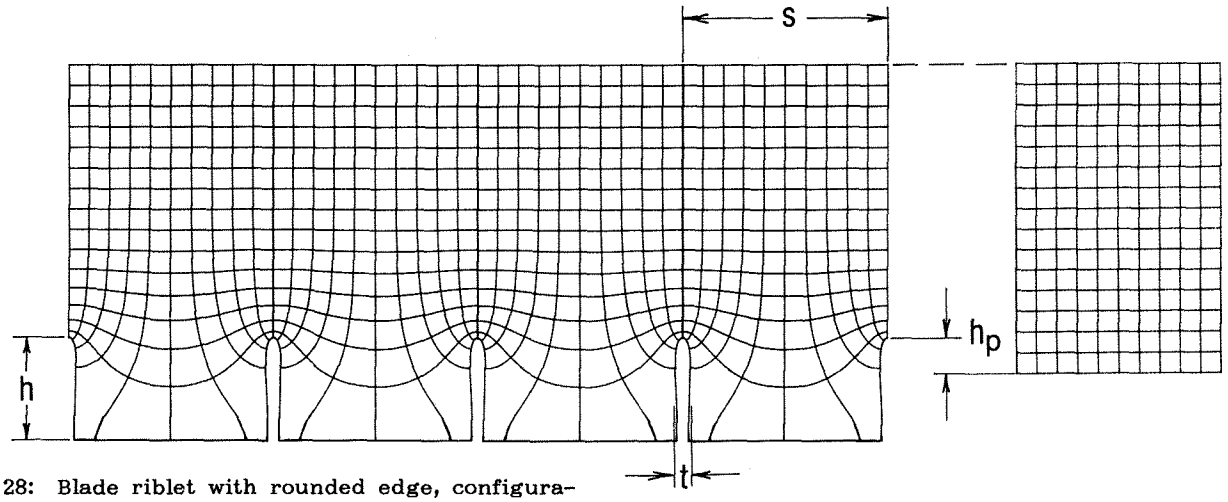

Fig. 28: Blade riblet with rounded edge, configuration and flow distribution. Riblet height h/s = 0.50, parameter a/b = 0.773, protrusion height h_p/s = 0.179, maximum thickness t/s = 0.0740.

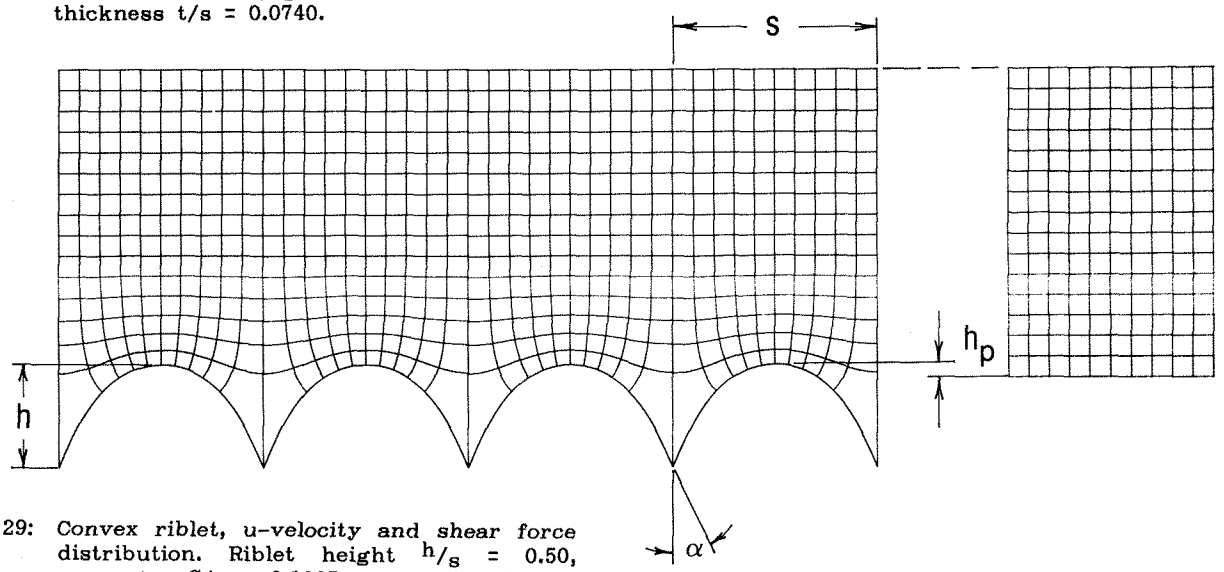

Fig. 29: Convex riblet, u-velocity and shear force distribution. Riblet height h/s = 0.50, parameter α/π = 0.1305, protrusion height h_p/s = 0.0724.

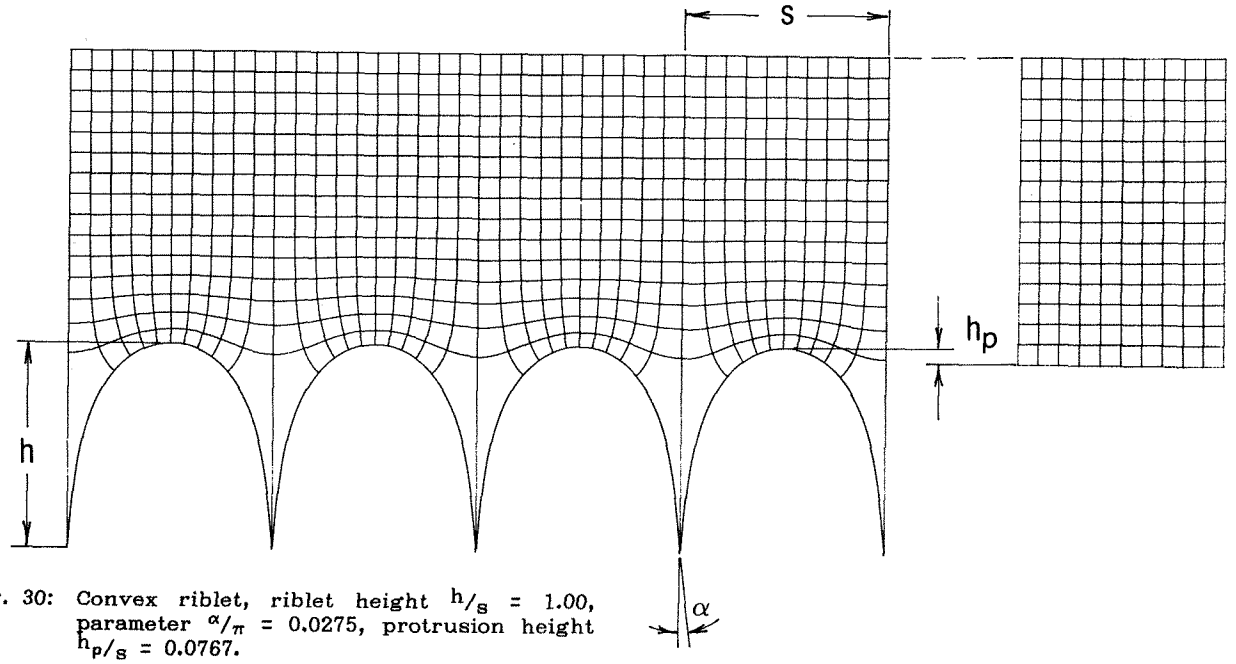

Fig. 30: Convex riblet, riblet height h/s = 1.00, parameter α/π = 0.0275, protrusion height h_p/s = 0.0767.

Fig. 31: Short three-dimensional riblets in a staggered array.

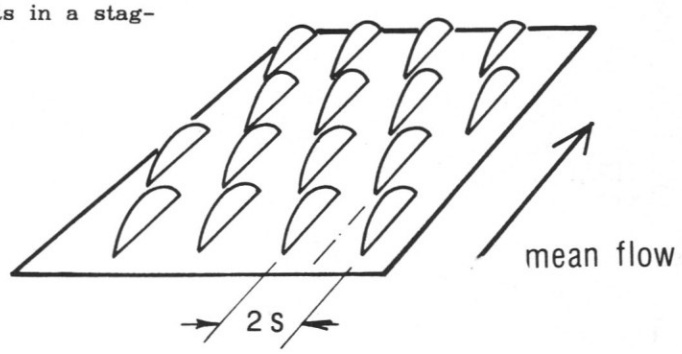

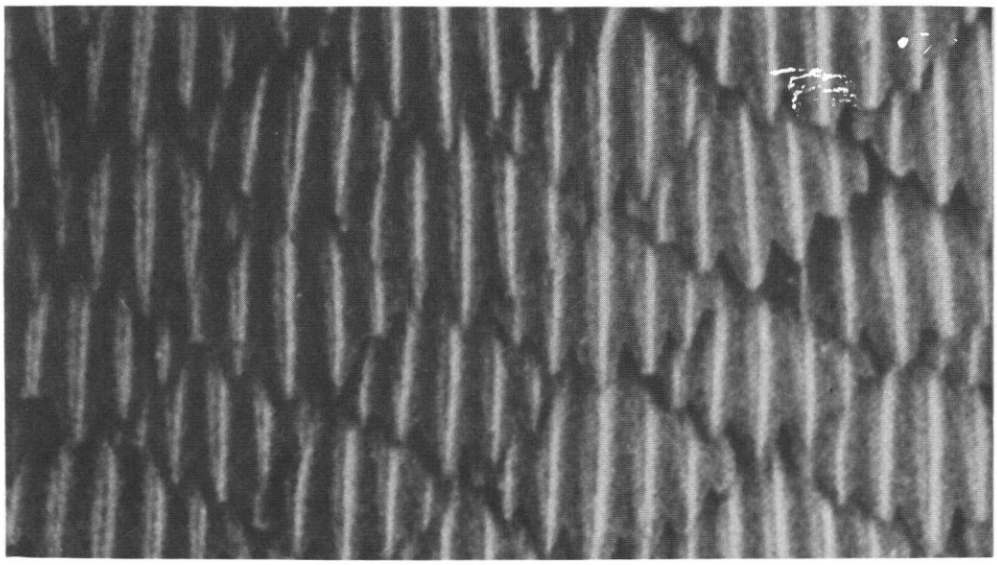

Fig. 32: Interlocking scales with staggered riblets on a hammerhead shark.

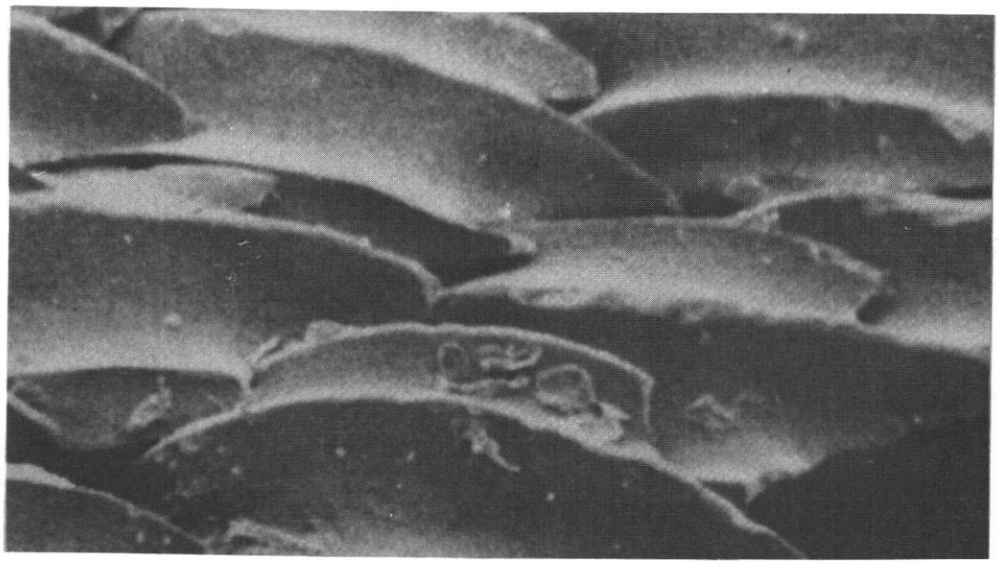

Fig. 33: Interlocking scales with staggered riblets on a great white shark.

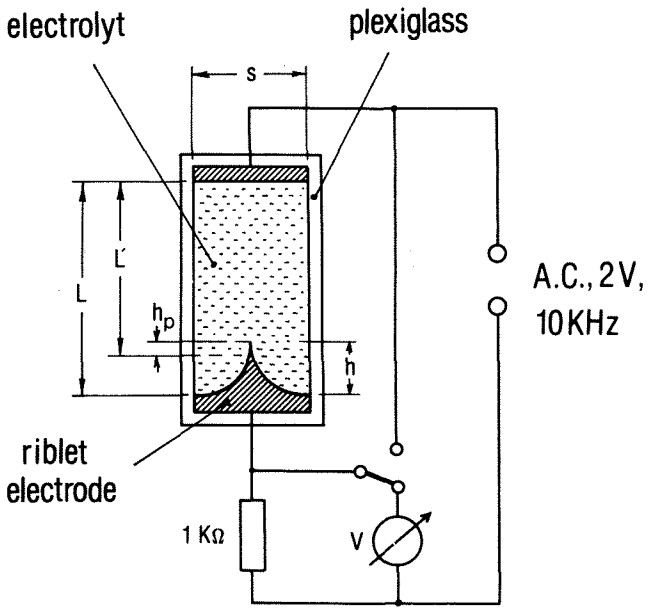

Fig. 34: Schematic diagram of the electrolytic experiment.

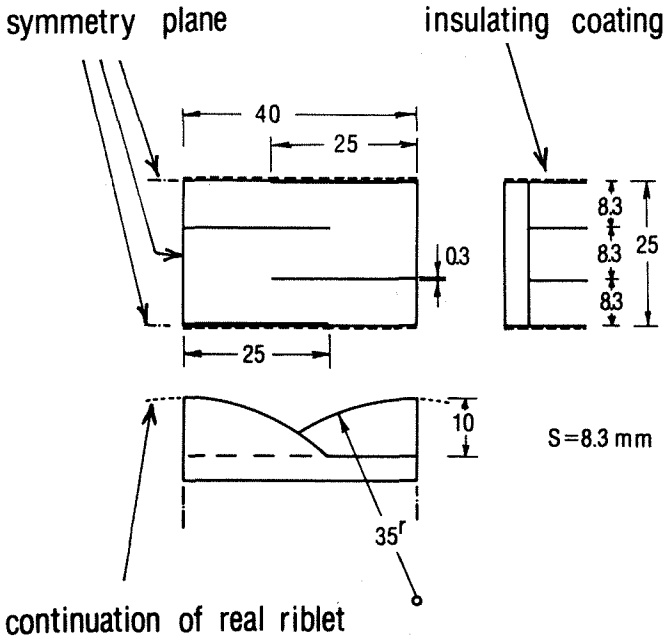

Fig. 36: Dimensions of the three-dimensional riblet demonstration electrode.

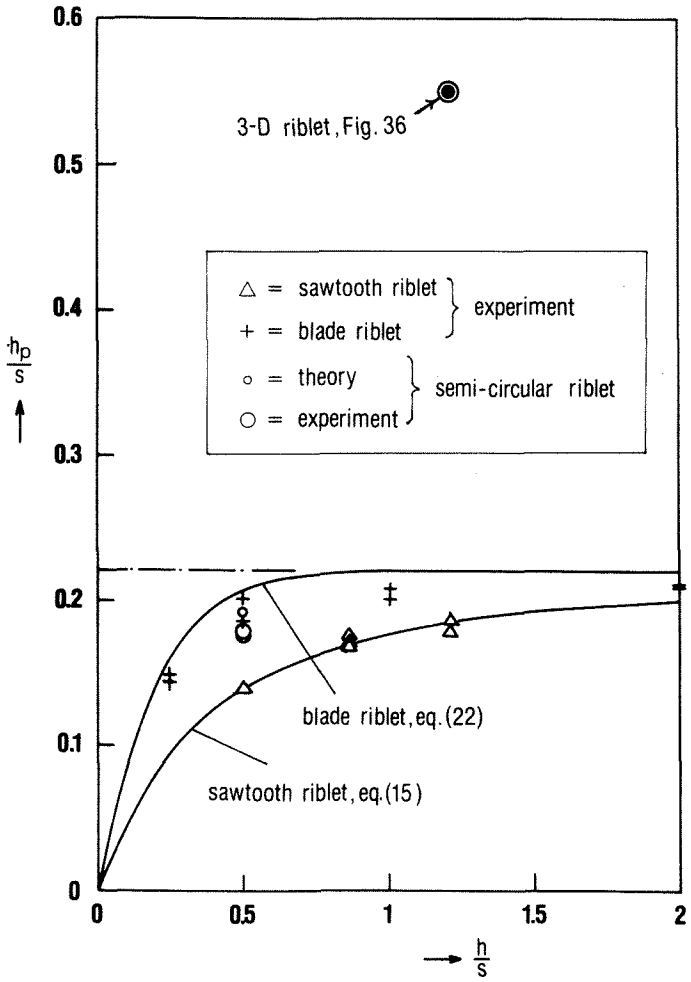

Fig. 35: Protrusion height. Electrolytic experiments versus theory.

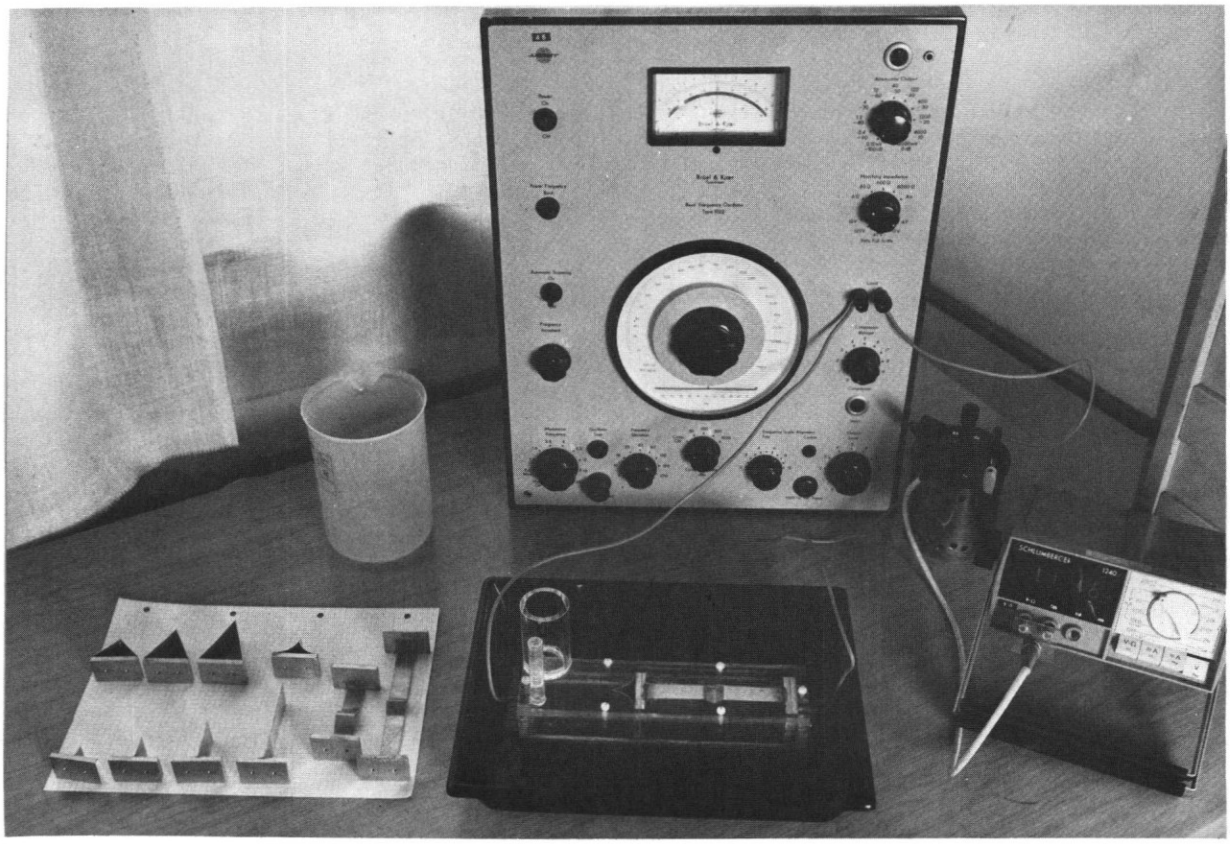

Fig. 37: Setup of the electrolytic experiments.